Behavior of Electrified Metal Surface in Contact with Aqueous Solution revealed by In-Situ Atomic Force Microscopy

2000

Nobumitsu Hirai

Contents

Chapter 1.

General Introduction

I. Scope of this study

Recently, importance of miniaturized electronic devices with high performance and low cost has attracted a growing interest year by year. Techniques to grow ultra thin and epitaxial films with atomical flatness are essential for making such devices. These ultra thin films have been produced mostly in vacuum up to now. Especially, by using molecular beam epitaxy (MBE) method [1], thickness and composition of such atomically flat, ultra thin and epitaxial films can be controlled very precisely.

On the other hand, except for film deposition in solution at a relatively high rate, that is, "plating", studies of ultra thin film deposition in solution have not gotten as far as those in vacuum, because of the difficulty in exposing well-ordered surfaces in solution and of the lack of *in-situ* techniques to obtain local information about the surfaces in solution on an atomic scale. Since Binnig and his co-workers invented scanning tunneling microscope (STM) [2] and atomic force microscope (AFM) [3], however, many researchers have investigated the surfaces with atomic resolution in solution, as well as in vacuum, and it was found that clean and bare surfaces of noble metals could be easily obtained even in solution.

One of the best advantages of wet processes in comparison with dry processes is that we can control the electric field, which can increase up to 10^7 V cm $^{-1}$, at electrode/ electrolyte interface by means of the potential of the electrode, e. g. 1 V, as shown in Fig. 1-1. It is expected that the influence of such a high electric field on the mobility of atoms on surfaces is not so small in comparison with the electric field of $(1\sim7)\times10^8$ V cm $^{-1}$ [4], which causes for the atoms on surfaces to be evaporated in vacuum. Surface physics under such a high electric field is interesting from both theoretical and practical viewpoints, although some complexity exists in solution, such as specific adsorption of anions, diffusion or migration of reactants in solution, and so on.

Based on these points of view, I have investigated metal surfaces in aqueous solution under the control of potential by means of *in-situ* electrochemical AFM (EC-AFM). Target for

this investigation is the behavior of electrified metal surfaces in contact with aqueous solution.

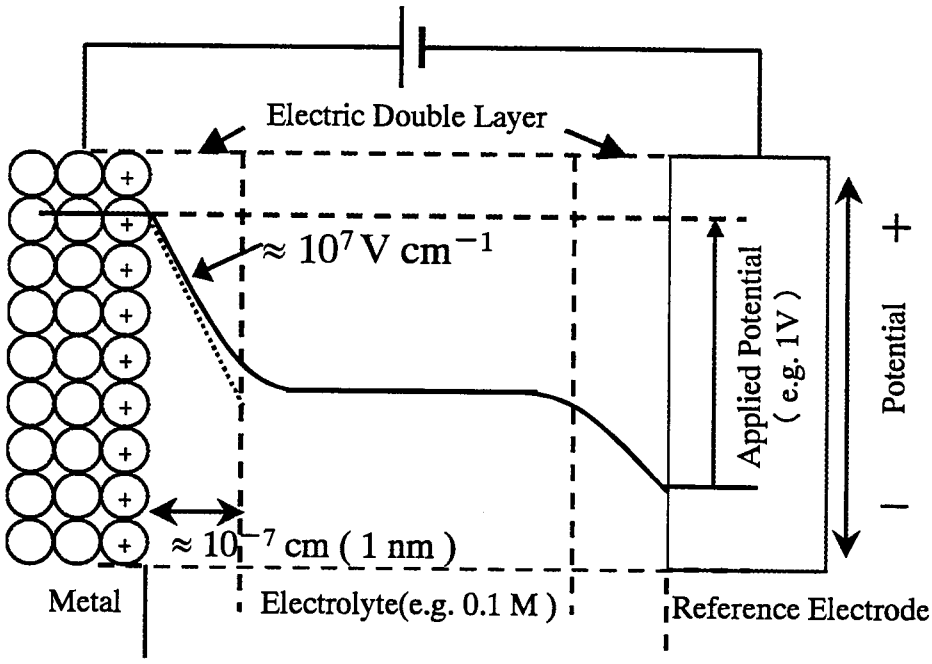

Figure 1-1 Schematic illustration of "metal-electrolyte interface" under the control of potential with disregard for size and specific adsorption of electrolytic ions, that is, the Gouy-Chapman diffuse charge model of the electric double layer or the ionic-cloud theory [5]. Distribution of applied potential is also shown in this figure schematically.

II. Composition of the thesis

This thesis is structured as the following:

Chapters 2 and 3 show two examples of relaxation processes of clean metal surfaces in aqueous solution under the control of potential, namely, decay of islands on Au(100) and (111) surface in the Chap. 2 and that of holes on Ag(100) surface in the Chap. 3, respectively. Effects of a surface excess charge and a high electric field at metal/ electrolyte interface on these relaxation processes are discussed.

In Chapter 4, initial stages of adsorption of benzotriazole on copper single crystals in aqueous solution are investigated by electrochemical methods and *in-situ* EC-AFM. Epitaxial relationships between the copper single crystals and adsorbed films of benzotriazole are discussed.

In Chapter 5, an initial stage of anodic oxidation of Fe(110) surface in aqueous solution is

investigated by electrochemical methods and *in-situ* EC-AFM. An epitaxial relationship between the Fe(110) substrate and an anodic oxide film is discussed.

Chapter 6 shows trials of electrodeposition of II – IV semiconductor ultra thin films on gold single crystals, which are investigated by electrochemical methods and X-ray Photoelectron Spectroscopy (XPS).

Finally, the thesis is summarized in Chapter 7.

References

[1] J. R. Arthur and J. J. LePore, J. Vac. Sci. & Technol. **6** (1969) 545.

[2] G. Binnig, H. Rohrer, Ch. Gerber and E. Weibel, Phys. Rev. Lett., **49** (1982) 57.

[3] G. Binnig, C. F. Quate and Ch. Gerber, Phys. Rev. Lett., **56** (1986) 930.

[4] O. Nishikawa, Kagaku, **49** (1979) 19.

[5] J. O' M. Bockris and A. K. N. Reddy, Modern Electrochemistry, Plenum Publishing Corp., New York (1970).

Chapter 2.

Decay of Islands Located on Au(100) and Au(111) in Contact with Aqueous Solution under the Control of Potential

I. Introduction

Surface diffusion is one of the most interesting issues in science during this century. Since Volmer *et al.* discussed the process of diffusion on surfaces in their experiments on crystal growth [1], many researchers have investigated the self-diffusion processes on metal surfaces by means of various experimental methods. These methods can generally be classified in two different groups, tracer diffusion methods and collective diffusion methods [2,3]. The former are the methods observing the migration of distinguishable atoms on surfaces, such as radioactive tracer experiments, field ion microscopy (FIM) [4] and STM. The latter are those observing the concentration profile of atoms, $c(x, t)$, when the system, which is either in equilibrium or in non-equilibrium, evolves from one configuration to another.

As well as various experimental studies shown above, several theoretical studies of surface diffusion have been made up to now. The principles of thermodynamics was first applied by Herring to the collective diffusion processes and he has established the thermodynamic expression for geometrical equilibrium of the solid-vacuum interface as follows [5,6]:

$$\mu_M - \mu_0 = \Omega \left[\gamma \left(\frac{1}{R_1} + \frac{1}{R_2} \right) + \frac{1}{R_1} \frac{\partial^2 \gamma}{\partial n_1^2} + \frac{1}{R_2} \frac{\partial^2 \gamma}{\partial n_2^2} - P_{xx} \right], \qquad (2\text{-}1)$$

where μ_M: chemical potential at the point M just beneath the surface [J/atom]

μ_0: chemical potential just beneath a flat surface [J/atom]

Ω : atomic volume [m^3/atom]

γ: local surface tension [J/m^2]

R_1, R_2: principal radii of curvature [m]

n_1, n_2: surface directions associated with the principal radii of curvature

P_{xx} : externally applied traction [N/m^2].

Models to describe crystal surfaces on an atomic scale are important in order to account for the experimental data and their dependence on orientation and temperature. Terrace-ledge-kink (TLK) model [7] is one of these models . Furthermore, various approximate (Morse potential, Lennard-Jones potential, embedded atom methods or effective medium theories) and ab initio (density functional theories) techniques have been utilized in order to estimate activation energies of individual steps of surface diffusion.

A great deal of understanding of surface diffusion has been achieved in each works shown above, however, a comprehensive understanding of strong connection between the atomistic information and the collective phenomena is still lacking.

Meanwhile, surface diffusion processes in electrolytes have not been investigated until the last two decades, because of the lack of the equipment for direst observation of the surfaces in solution. After the invention of STM and AFM, which can be applied to the *in-situ* observation of the surfaces in aqueous solution, a few studies of the change of surface morphology with time in various electrolytes have been investigated by *in-situ* EC-STM [8-11] and EC-AFM [12, 13]. They demonstrated that a rapid surface diffusion occurred on gold single crystals in aqueous solution at a certain potential. However, there is a discrepancy in their results and universal theories of surface diffusion of metal in contact with electrolyte, which involves the effects of the given potential, the electrolyte and the orientation of metal electrode, etc, have not been established yet. From such a standpoint, Ikemiya *et al.* have reported strong potential dependence of the decay rate of small holes located on Au(100) single crystals in 0.05 M H_2SO_4 aqueous solution [14].

In this Chapter, I investigate the decay of homogenous multi-layered islands atop of the terrace on substrates in 0.05 M H_2SO_4 aqueous solution under the control of potential at room temperature by *in-situ* EC-AFM. The substrates used here are Au (100) and Au(111) single crystals because their clean and bare surfaces can be obtained easily in solution. The decay of islands on surfaces of gold [15,16], silver [17-19], or silicon [20-26] single crystals in contact with vacuum or air has been observed experimentally and the mechanism of the decay have become gradually clear, not perfectly, owing to the comparison of these experimental works with theoretical consideration [18,27-30]. Therefore, one of the most important discussion in this chapter is the comparison between my results and the previous works which should result in more

profound understanding of both the decay of homogenous islands on surfaces in any circumstances and the effect of keeping potential at metal-electrolyte interface.

II. Experimental

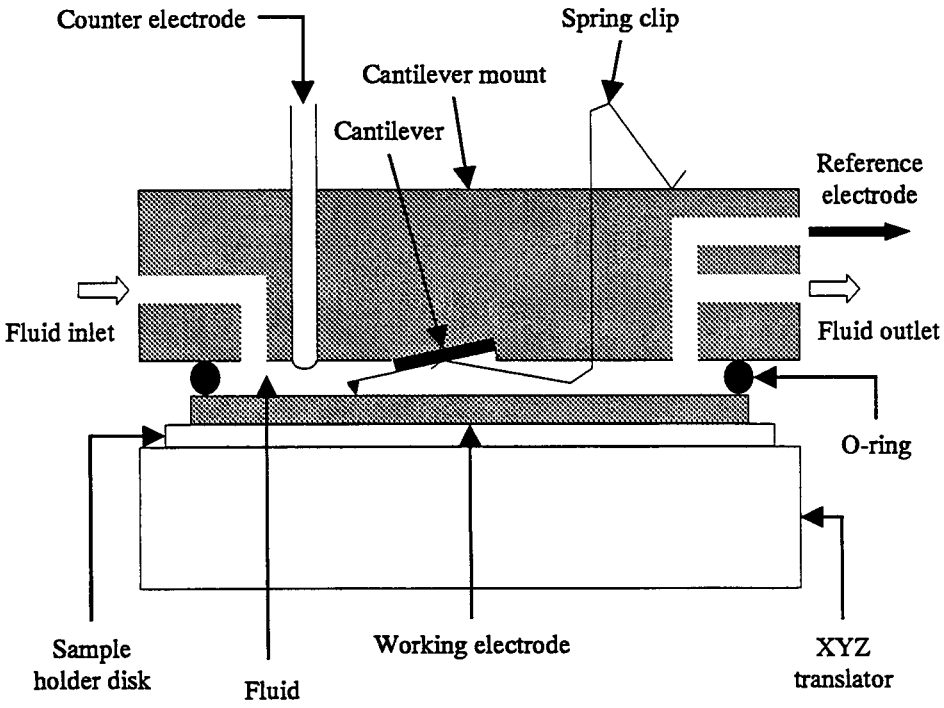

Figure 2-1 Schematic diagram of cross section of the electrochemical AFM cell.

A single crystal Au rod (disk, 12 mm diameter) was grown by Bridgman method. Orientation of the samples was verified within $\pm 1^\circ$ by Laue backscattering method. After mechanically polished, the samples were electropolished in a solution of 10 ml of HCl and 90 ml of C_2H_5OH for 30 minutes in order to remove damaged layers made by the mechanical polishing. *In-situ* EC-AFM images are taken by Nanoscope E (Digital Instruments, Inc.). Figure 2-1 shows a cross section of the EC-AFM cell. The potential of a working electrode was controlled by a potentiostat and was referred to a reference electrode. Although the reference electrode actually used here was Hg/Hg_2SO_4 electrode (0.65 V vs. normal hydrogen electrode; NHE), all potential were referred to NHE in this chapter. The space surrounded by the working electrode, a cantilever mount and an O-ring was filled with an electrolyte. The electrolyte used was 0.05 M H_2SO_4 aqueous solution (pH = 1.1), which was prepared from H_2SO_4 (Wako, Superior) and MilliQ-water. The electrolyte was deaerated with Ar gas for more than 1 hour before each

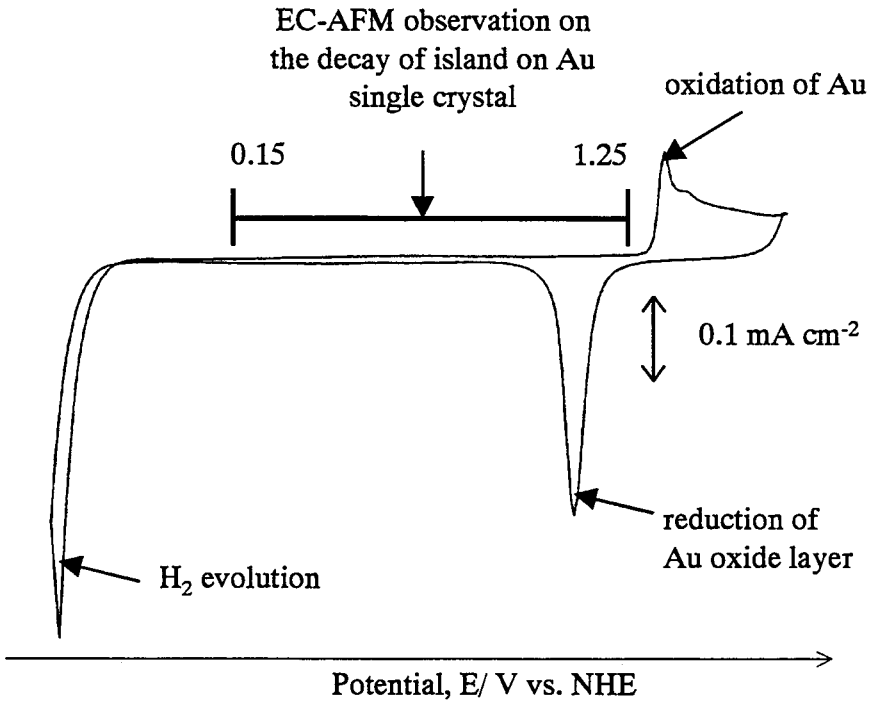

Figure 2-2 Cyclic voltammogram on Au(100) single crystal in 0.05 M H_2SO_4 aqueous solution with scan rate of 50 mV sec^{-1}. The keeping potential range for observation of the decay process of island is also shown in this figure.

experiment. All of the experiments were performed at room temperature. Figure 2-2 shows a cyclic voltammogram (CV) on Au(100) single crystal in 0.05 M H_2SO_4 aqueous solution, accompanied with the indication of potential range for observation of the decay process of an island. In this potential region, no reaction current was detected.

III. Results

Figures 2-3(a)-(e) indicate a time-lapse sequence of *in-situ* AFM images showing the decay of a homogenous multi-layered island located on Au(111) single crystal at 1.05 V in 0.05 M H_2SO_4 aqueous solution. The structure in Fig. 2-3(a), which is composed of terraces and mono-atomic steps, was prepared by sweeping the potential a hundred times between 0.65 V to 1.65 V for 1 hour in the same solution. The first layer of the island disappeared within 144 seconds. The shape of the island is a triangle or a hexagon and it is found that the direction of step edges is $<1\bar{1}\ 0>$, that is revealed by the atomic resolution image, shown in Fig.2-3(f).

Figure 2-4 shows that the number of atoms in the first layer, which is calculated from the

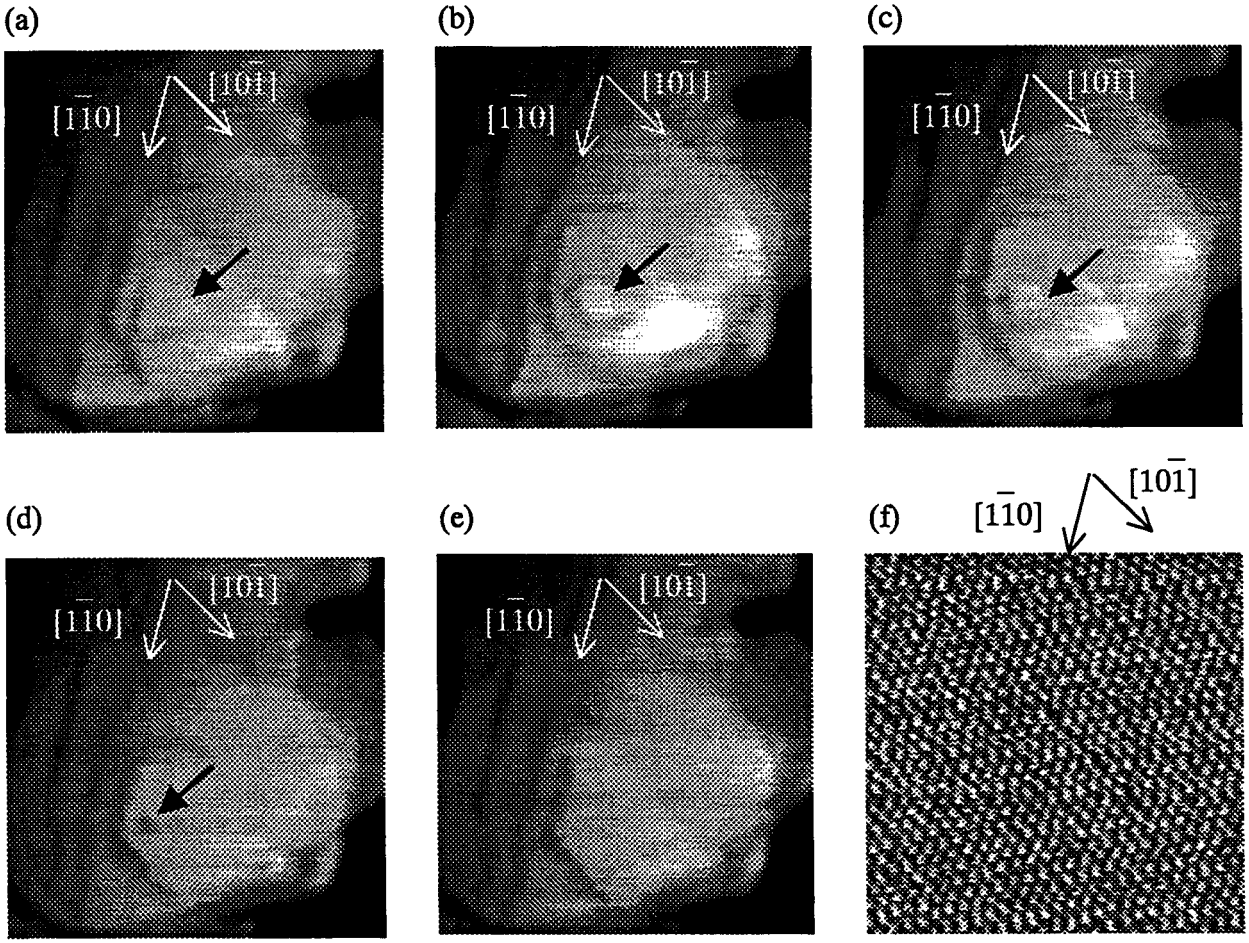

Figure 2-3 Series of AFM images (a)-(e) (310×310 nm) showing the decay of an island on Au(111) electrodes at 1.05 V in 0.05 M H_2SO_4 aqueous solution at room temperature. Image(a) was taken immediately after creating the island. The subsequent images were obtained (b)32s, (c)63s, (d)110s, and (e)144s after image(a). Image(f) is an atomic resolution image (8.1×8.1 nm) observed on the terrace, which is shown in Fig. 2-3(e)

area of the first layer, decreases linearly with time. In the figure, decay lines for Au(100) and Au(111) plane at 1.05 V in 0.05 M H_2SO_4 aqueous solution are shown and those are compared with that for observed on Au(111) in air measured by Cooper *et al.* [15,16]. In all the cases, the areas decrease linearly with time. It is noteworthy that the decay rate (= slope of decay lines) for Au(100) at 1.05 V in 0.05 M H_2SO_4 aqueous solution is 820 atom/sec, which is about 5 times higher than that for Au(111) and more than 100 times higher than that for Au(111) in air reported.

The decay of the second and third layers (see Fig. 2-5(a)), as well as the first layer, of a

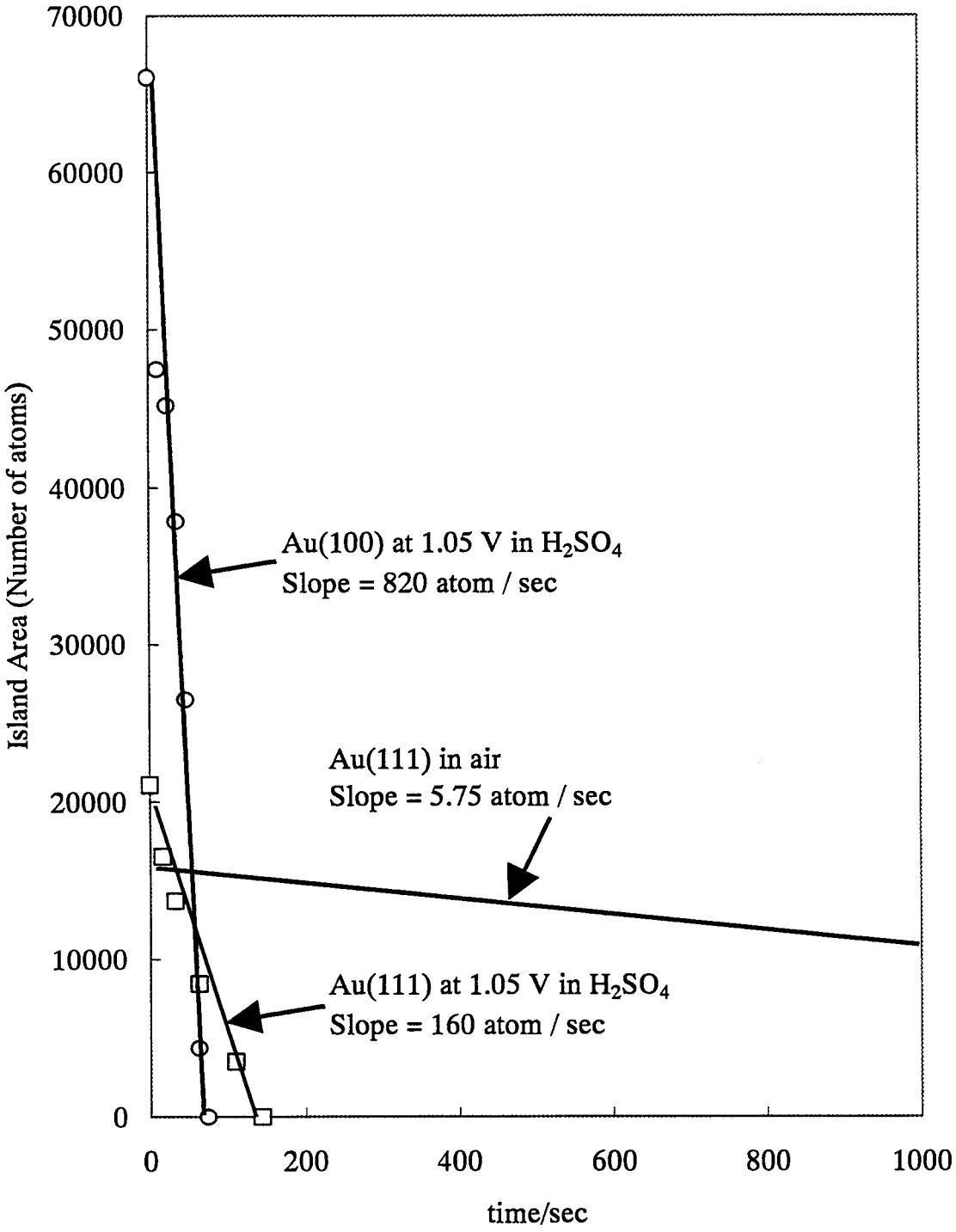

Figure 2-4 Time-dependence of the number of atoms in the first layer on Au single crystals in 0.05 M H_2SO_4 aqueous solution. The number of atoms is calculated from the area of the first layer and it is compared with that on Au(111) in air observed by Cooper *et al.* [15, 16].

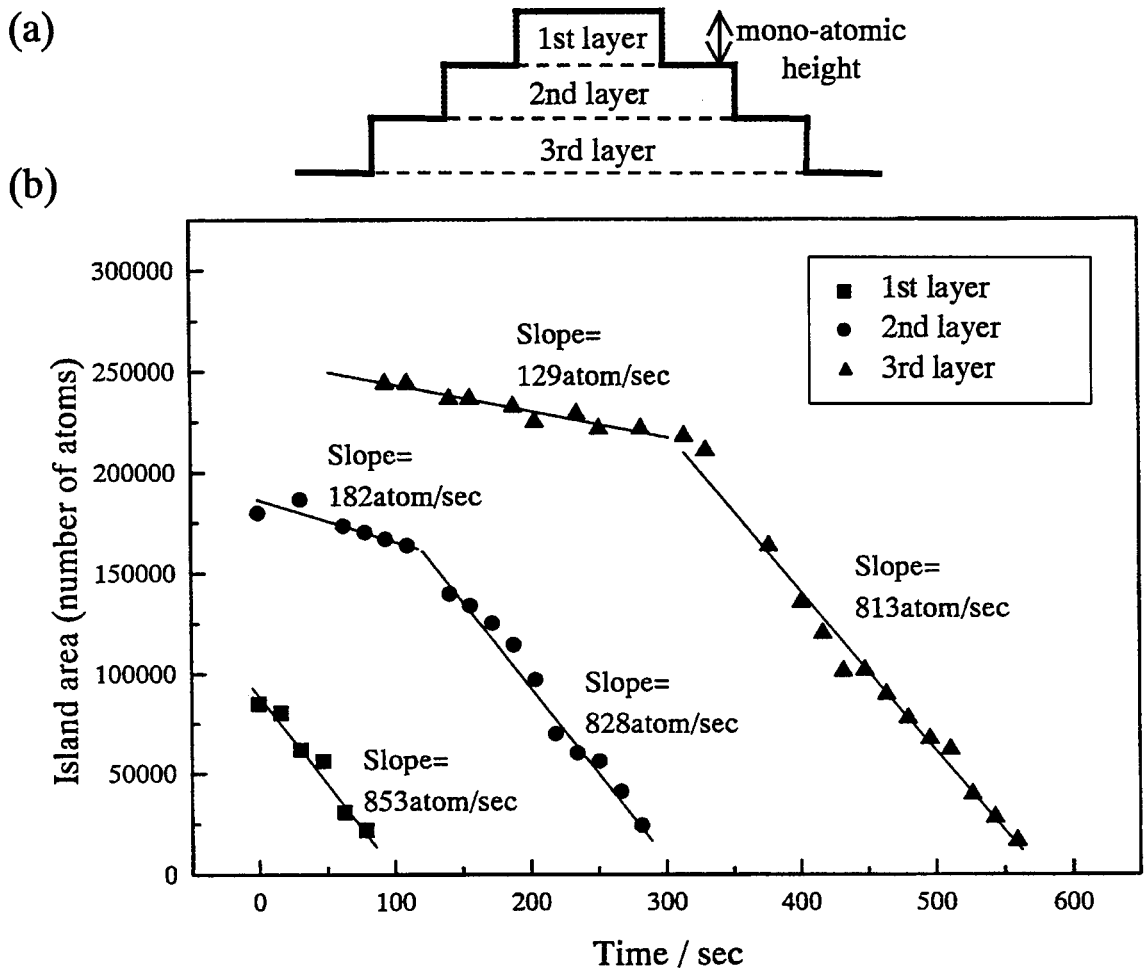

Figure 2-5 (a) Schematic diagram of cross section of a multi-layered island and (b) time-dependence of areas of the 1st, 2nd and 3rd layers of an island on Au(100) at 1.05 V in 0.05 M H_2SO_4 aqueous solution.

multi-layered island located on Au(100) single crystal was also observed. Figure 2-5(b) shows the relationship between the area of each layer and the time. As shown in Fig.2-5(b), the decay of the lower layer before the complete collapse of the upper layer is faster than that after the complete collapse of the upper layer, suggesting that this decay process is mainly caused by the surface diffusion of atoms on the surface from the upper layer to the lower layer, not by the dissolution of atoms at the kink site into solution.

Figure 2-6 shows the decay rate of the island on the Au surface in 0.05 M H_2SO_4 aqueous solution as a function of applied potential, indicating that the more positive the potential became between 0.15 V and 1.2 V, the more rapid decay of islands was observed.

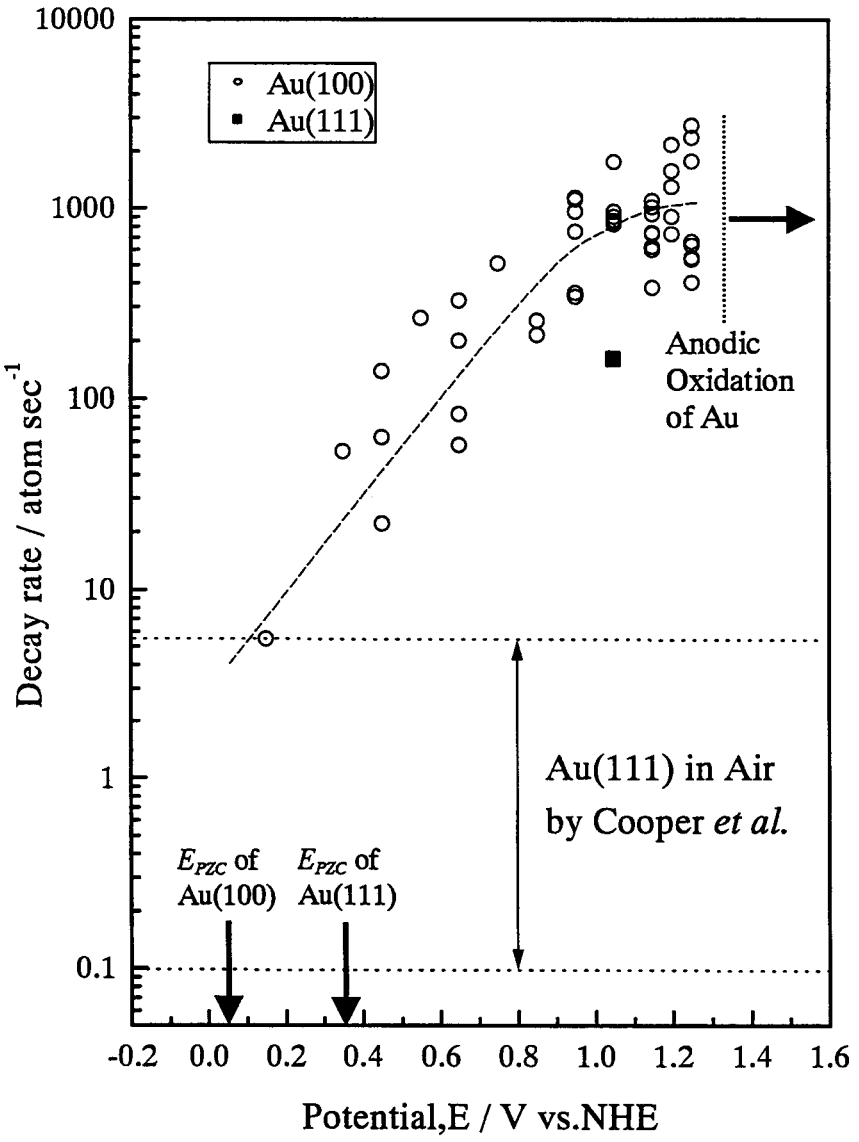

Figure 2-6 Decay rate of the first layer of islands on the Au (100) and Au(111) surfaces in 0.05 M H_2SO_4 aqueous solution as a function of applied potential.

IV. Discussion

IV-1. Mechanism of the decay of islands

As mentioned in the last paragraph, the decay of the islands observed in the present work is mainly caused by the surface diffusion of atoms on the surface from the upper layer to the lower layer, not by the dissolution of atoms at the kink site into solution, so it's interesting to compare the present works with the previous experimental works in vacuum or in air. Therefore, the previous works about theoretical consideration [18,27-30] can be also applied to the present

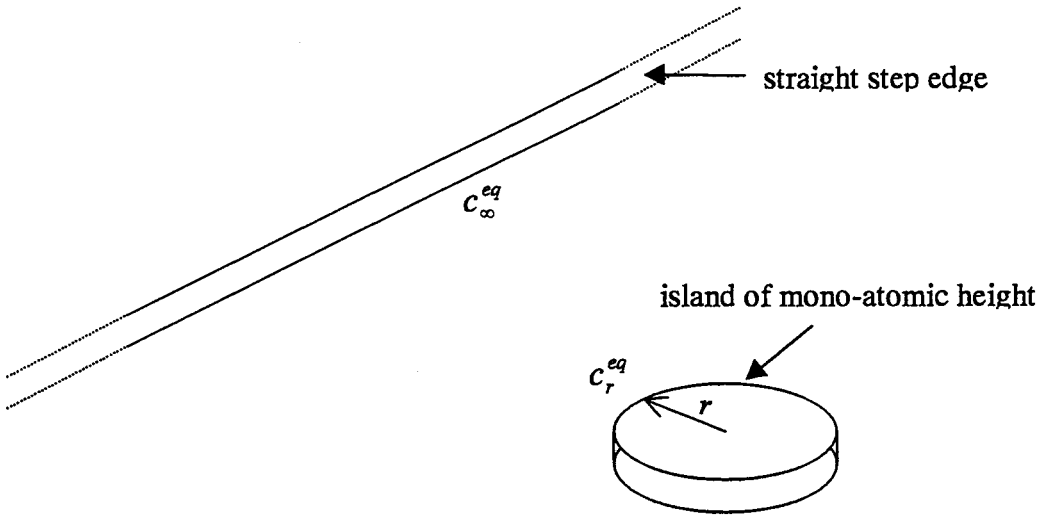

Figure 2-7 Schematic representation of an island of mono-atomic height and a straight step edge located on a surface.

work. There are two fundamentally different approach to describe the decay of islands, namely, macroscopic and microscopic treatments.

First, I describe the macroscopic diffusion mechanism. The key of the macroscopic consideration is the Gibbs-Thomson relation. The equilibrium adatom density c_r^{eq} just outside an island of radius r is given by the following equation,

$$c_r^{eq} = c_\infty^{eq} \exp\left(\frac{\gamma \Omega}{rkT}\right), \tag{2-2}$$

where c_∞^{eq} is the equilibrium adatom density just outside a straight step edge, γ is the edge free energy per unit of length, Ω is the area occupied by one atom in the island, k is Boltzmann's constant, and T is the absolute temperature (see Fig. 2-7 and Appendix 2.1).

On an actual surface in my work, there are many islands, which are formed as the result of surface roughening by sweeping the potential a hundred times between 0.65 V to 1.65 V for 1 hour in 0.05 M H_2SO_4 aqueous solution, with various curvatures and the islands which I have observed in my work usually have comparatively small radii of curvatures. Thus, the areas of them decrease with time because the actual adatom density just outside them is much smaller than c_r^{eq}.

Under such condition described above, the schematic representation of a cross section of the island and the adatom density around it can be illustrated as shown in Fig. 2-8 for the

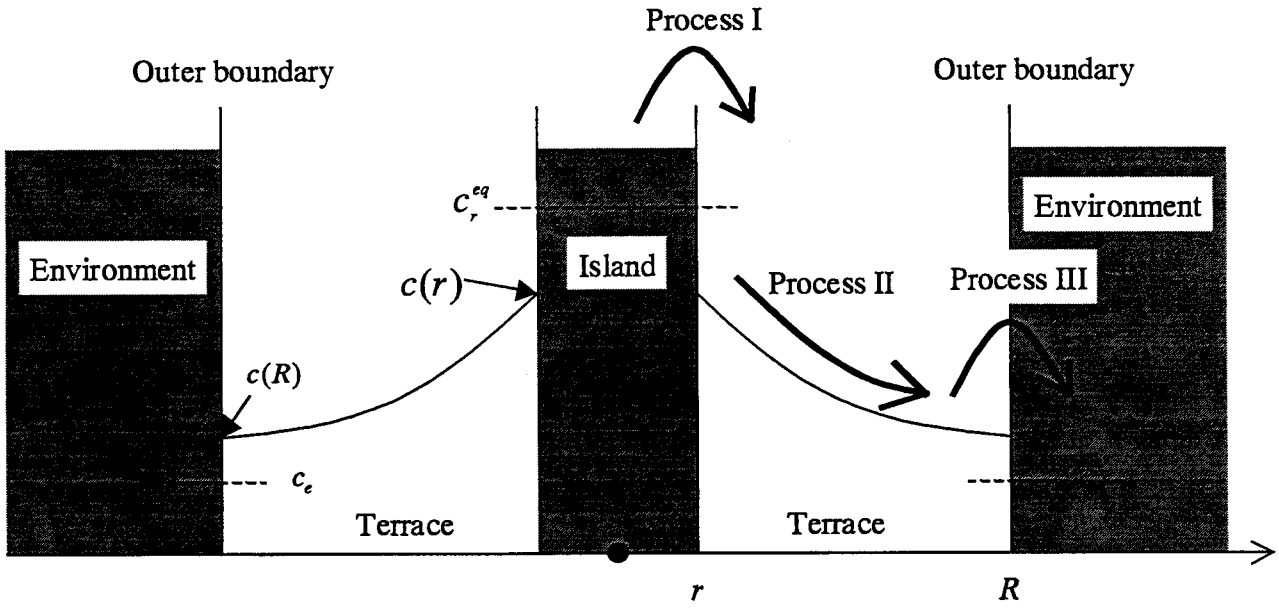

Figure 2-8 Schematic representation of a cross section of the island accompanied with the adatom density around it. The current of its decay are also shown by arrows.

continuum model, which was applied to the discussion in the previous work [29]. In this figure, r is a radius of the island, R is the imaginary radial distance from the center of the island to the "outer boundary", $c(\tilde{r})$ is the actual adatom density as a function of the radial distance $\tilde{r}$ from the center of the island, and c_e is the actual adatom density in the "environment". From this model, it is considered that the decay process of an island consists of the following three processes: detachment of atoms from the step edge (Process I), diffusion of atoms across the terrace (Process II), capturing atoms to the "environment" (Process III), as also shown in Fig. 2-8.

In Process I, II and III, the atom currents J_I, J_{II} and J_{III} are given by the following equations;

$$J_I = 2\pi r K_I \left(c_r^{eq} - c(r)\right), \tag{2-3}$$

$$J_{II} = 2\pi \frac{K_{II}}{\ln(R/r)} \left(c(r) - c(R)\right), \tag{2-4}$$

$$J_{III} = 2\pi R K_{III} \left(c(r) - c_e\right), \tag{2-5}$$

respectively, where K_I, K_{II} and K_{III} are the constants. In the steady state, the three atom currents must be equal, and hence the atom current $J (= J_I = J_{II} = J_{III})$ is as follows;

$$J = 2\pi \mathrm{K(r)} \left(c_r^{eq} - c_e\right) = 2\pi \mathrm{K(r)}\, c_\infty^{eq} \left[\exp\left(\frac{\gamma\, \Omega}{rkT}\right) - \frac{c_e}{c_\infty^{er}} \right], \tag{2-6}$$

where

$$K(r) \equiv \left(\frac{1}{K_I r} + \frac{1}{K_{II}} + \frac{1}{K_{III} R} \right)^{-1}. \tag{2-7}$$

In case that the exponential factor of Eq. (2-6) is much smaller than one and c_e^{eq} is close enough to c_∞^{eq}, Eq. (2-7) gives the following expression;

$$J \cong 2\pi K(r) c_\infty^{eq} \left[\left(1 + \frac{\gamma\, \Omega}{rkT}\right) - 1 \right] = \frac{2\pi K(r) c_\infty^{eq} \gamma\, \Omega}{rkT} \propto \frac{K(r)}{r}. \tag{2-8}$$

Now, consider the limiting process in the decay of an island. If it is assumed that the detachment of atoms from the step edge (Process I) is the limiting process in the decay of an island, in other words, it is assumed that K_I is much smaller than K_{II} and K_{III}, $K(r)$ is proportional to r and J is constant with r. It is considered that my work and some previous works [22] are in this case, because the area of an island decreases linearly with time. On the other hand, assuming that the diffusion of atoms across the terrace (Process II) is the limiting process, $K(r)$ is constant with r and J is proportional to $1/r$ in case that $\ln(R/r)$ can be considered constant. It is considered that the other works [26] are in this case. It is noteworthy that there remains contradiction of the limiting process in the previous works [22,26] even though the material (Si(111)) and the measured temperature range are same in both experiments. The fact suggests that it is indispensable to take account of the effects of all kinds of experimental conditions, such as the imaginary radial distance from the center of the island to the "outer boundary", the actual adatom density in the "environment", and so on.

Second, I discuss the microscopic approach only briefly. In the macroscopic discussion described above, it is assumed that the island is isotropic and its shape is real circle, however, the shape of the actual islands, whose edges are consist of ledges and kinks, is not a real circle but a polygon, as shown in Fig. 2-3, and it is important to consider the effects of the various sites. The number of atoms at the ledge is proportional to $1/r$, whereas the one at the kink site is constant with r. Therefore, it is considered that only the atoms at the kink site of an island can leave the island if assuming that Process I is the limiting process in the decay of the island. This conclusion from the microscopic approach is consistent with the Gibbs-Thomson relation obtained in the

macroscopic consideration.

IV-2. Influence of applied potential upon the decay of islands

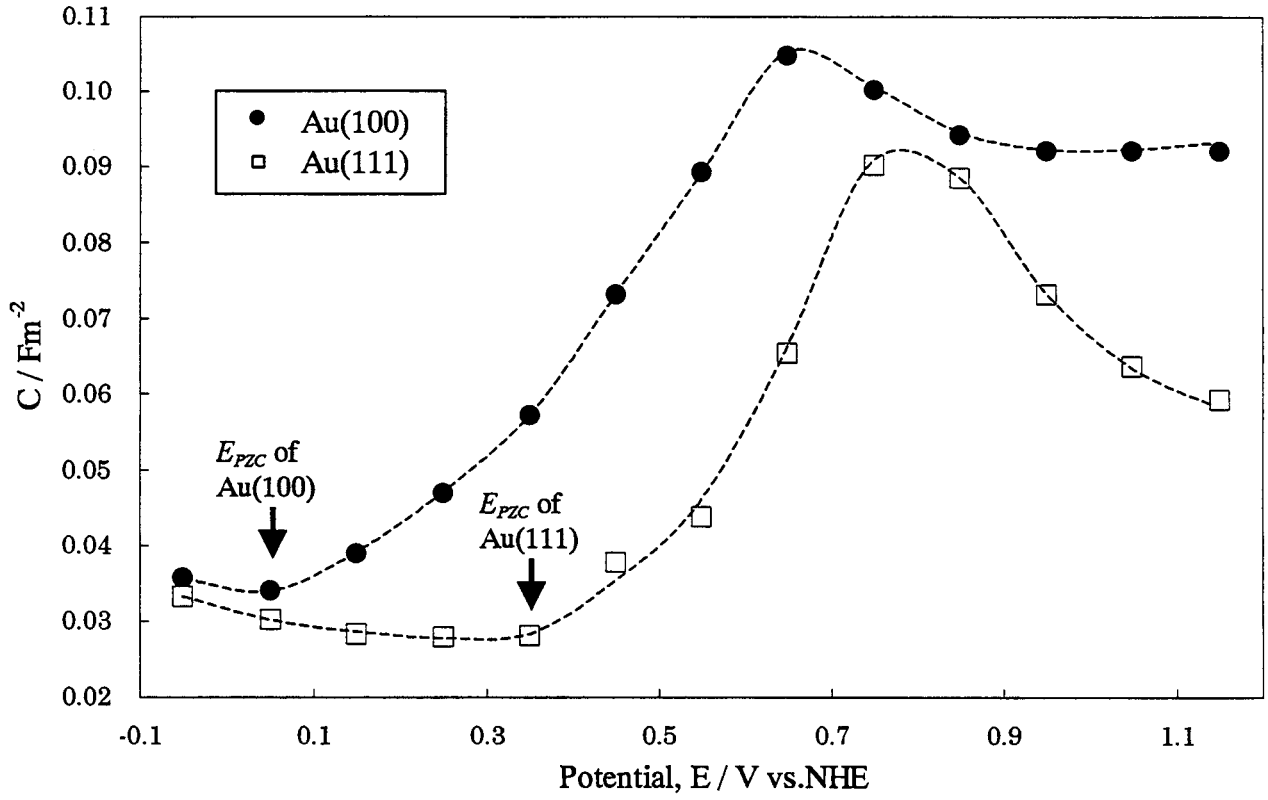

Figure 2-9 Differential capacitance of the Au(100) and Au(111) samples, which were utilized in the present work, in 0.05 M H_2SO_4 aqueous solution.

The most interesting discussion in this chapter is the influence of the potential of the substrate upon the decay of island located on the substrate. As shown in Fig. 2-6, the decay of islands becomes faster when the potential of Au(100) increases in the potential range between 0.15 V and 1.2 V. It is considered that the electric field at the electric double layer influence the decay process. Figure 2-9 shows the differential capacitance of the Au(100) and Au(111) samples, which were utilized in the present work, in 0.05 M H_2SO_4 aqueous solution, indicating that the potential of zero charge (E_{PZC}) of Au(100), which is considered the applied potential where the differential capacitance is minimum, is estimated to be approximately 0.05 V. Therefore, the electric field at metal/electrolyte interface increases with the applied potential in the potential range between 0.15 V and 1.2 V. If one assumes that the bulk of metal consist of electrons and

metal atoms taking a positive charge, the metal atoms at metal/electrolyte interface should be relaxed toward electrolyte by the electric field at metal/electrolyte interface and the atoms at the kink site can leave the island. In other words, c_{∞}^{eq} at higher potential is more than that at lower potential, so that the decay rate increases with the applied potential maintaining the relationship that the area of an island decreases linearly with time.

Until now, I have not succeeded in the quantitative treatment of the influence of the applied potential upon the decay of islands, however, I considered that it must be helpful for such treatment to measure the temperature dependence of the decay rate. The comparison of the decay rate in aqueous solution keeping at E_{PZC} with that in air is also interesting. The data are not enough now, however, it is considered that the decay rate in aqueous solution keeping at E_{PZC} is similar to that in air from Fig. 2-6.

IV-3. Influence of orientation upon the decay of islands

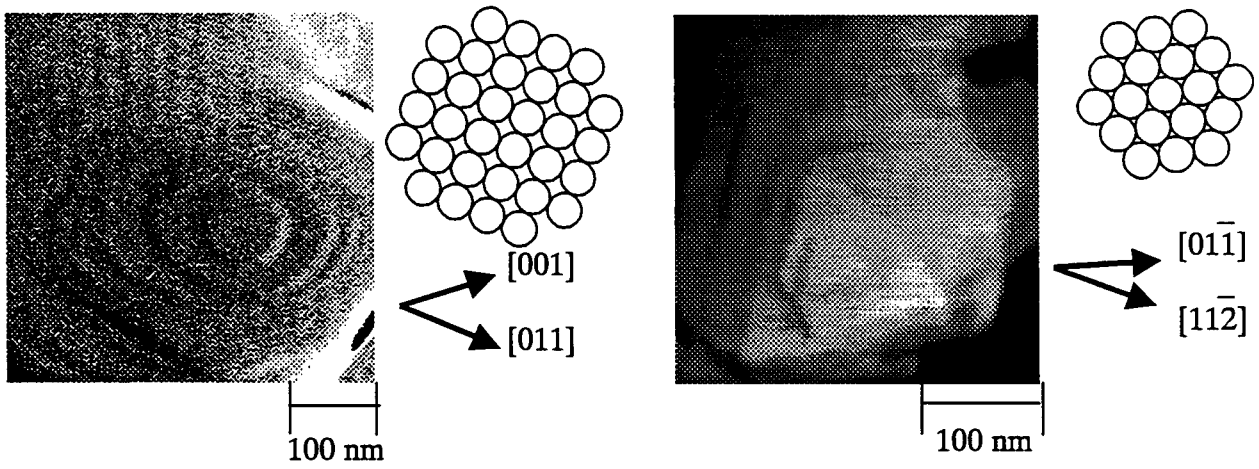

(a) Au(100) (b) Au(111)

Figure 2-10 AFM images of multi-layered islands located on (a) Au(100) and (b) Au(111), accompanied with schematic representation of the atomic resolution image of each orientation.

Figure 2-10 shows the AFM images of multi-layered islands located on (a) Au(100) and (b) Au(111), accompanied with the schematic representation of the atomic resolution image of each orientation. It is interesting that the islands are surrounded by the ledges with higher atomic density. In the case of Au(111), atomic density of the ledges of <01$\bar{1}$> direction is 3.47 atom/nm,

whereas that of the ledges of <11$\bar{2}$> is 2.00 atom/nm. Assuming that the easiness to leave the atoms governs the direction of the ledges surrounding the island, the island is surrounded by the ledges with lower atomic density. On the other hand, assuming that the island is surrounded by the ledges with more stability, the island is surrounded by the ledges with higher atomic density. In the present work, the island was surrounded by the ledges of <01$\bar{1}$>, so that the latter governs the direction of the ledges of the island. In the case of Au(100), the island was surrounded by the ledges of both <001> and <011>, probably because the difference of atomic density between the ledges of <001> and <011> on Au(100) is not so wide as that between the ledges of <01$\bar{1}$> and <11$\bar{2}$> on Au(111). Ye *et al.* observed the dissolution process of Au(111) substrate in perchloric acid solution involving a small amount of hydrochloric acid by *in-situ* STM, and the ledges of <01$\bar{1}$> were observed at negative potential than the dissolution potential, whereas the direction of the ledges changed from <01$\bar{1}$> into <11$\bar{2}$> at positive potential than the dissolution potential.

The difference between the decay rate for Au(100) and that for Au(111) can be explained by the effect of the electric field in the electric double layer, which has already been discussed in the last paragraph. Since the E_{PZC} of Au(111) is more positive than that of Au(100) as shown in Fig. 2-9, the electric field in the electric double layer on Au(111) at 1.05 V can be estimated to be

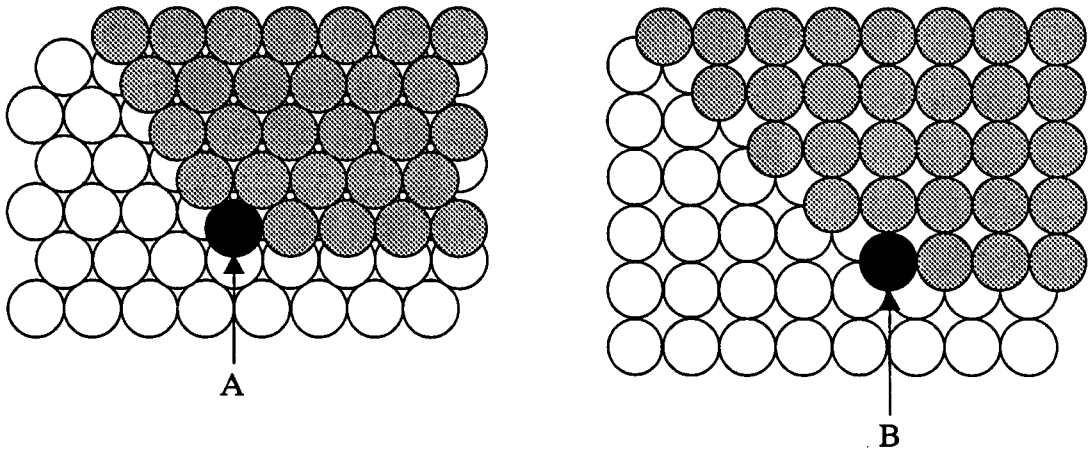

a) Au(111) b) Au(100)

Figure 2-11 Schematic diagrams of the atoms at the kink site on (a) Au(111) (site A) and (b) Au(100) (site B).

less than that on Au(100) at the same potential.

The difference between the decay rate for Au(100) and that for Au(111) also can be assigned to the number of the lateral neighbors of the atom at the kink site. Figure 2-11 shows the schematic diagrams of the atoms at the kink site on Au(111) and Au(100), which are going to leave from the kink site. The atom at the kink site on Au(111) (site A) has 3 lateral nearest neighbors, whereas the atom at the kite on Au(100) (site B) has 2 lateral nearest neighbors. Therefore, the atoms at the site B can leave more easily than those at the site A and the island on Au(100) can decays more rapidly than that on Au(111).

V. Conclusions

I investigated the decay of homogenous multi-layered islands atop of the terrace on Au (100) and Au(111) single crystals in 0.05 M H_2SO_4 aqueous solution under the control of potential at room temperature by *in-situ* EC-AFM.

The following conclusions were derived from the results and discussion:

1. The area of the first layer of islands decreases linearly with time at any applied potential. From this relationship, it is concluded that the detachment of atoms from the step edge is the limiting process in this decay of islands.
2. When the potential of Au(100) increases in the potential range between 0.15 V and 1.2 V, the decay of islands becomes faster. The decay for Au(111) at 1.05 V is more than 30 times faster than that in air reported. From these results, it is proposed that the metal atoms at metal/electrolyte interface are relaxed toward electrolyte by the electric field at the interface, which becomes higher at higher applied potential.
3. The islands are surrounded by the ledges with high atomic density.
4. The decay for Au(100) at 1.05 V is about 5 times faster than that for Au(111) at the same potential. This difference of the decay rate can be explained by the number of the lateral neighbors of the atom at the kink site and/ or by the effect of the electric field in the electric double layer.
5. The decay of the lower layer before the complete collapse of the upper layer is faster than that after the complete collapse of the upper layer. From this result, it is concluded that this decay process is mainly caused by the surface diffusion of atoms on the surface from the upper layer to the lower layer, not by the dissolution of atoms at the kink site into solution.

Appendix 2.1. Gibbs-Thomson relation

The Gibbs-Thomson relation, which is represented by Eq. (2-2)), is obtained in the following way.

The free energy ΔG to form a two dimensional island of radius r on a flat metal surface is given by the following equation;

$$\Delta G = \left(\mu_{M(island)} - \mu_{M(adatom)}\right)n + 2\pi r\,\gamma = \left(\mu_{M(island)} - \mu_{M(adatom)}\right)\frac{\pi r^2}{\Omega} + 2\pi r\,\gamma\,, \qquad (2\text{-}9)$$

where $\mu_{M(island)}$ is the chemical potential of an atom in the island, $\mu_{M(adatom)}$ is the one of an adatom on the surface, $n = \dfrac{\pi r^2}{\Omega}$ is the number of atoms in the island, Ω is an area occupied by an atom in the island, and γ is the edge free energy per unit of length, which is assumed to be isotropic and is independent of curvature. An atom in the island is more stable than an adatom, therefore, $\mu_{M(island)}$ is smaller than $\mu_{M(adatom)}$.

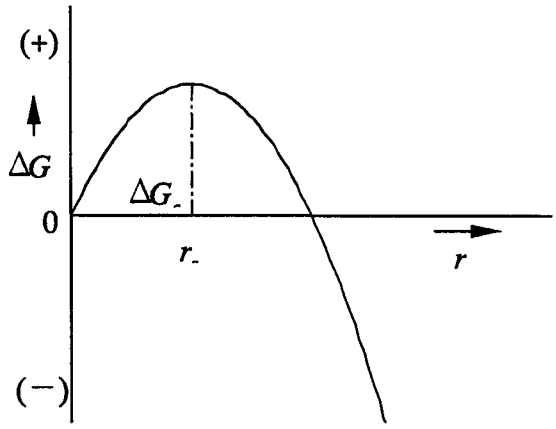

Figure 2-11 Schematic representation of the free energy ΔG to form an island of radius r.

Figure 2-11 shows schematic representation of the free energy ΔG to form an island of radius r. If the island is under "equilibrium", that is, the free energy ΔG is maximum and $\dfrac{d\Delta G}{dr} = 0$, the following equations are obtained;

$$\frac{d\Delta G}{dr} = \left(\mu_{M(island)} - \mu_{M(adatom)}\right)\frac{2\pi r}{\Omega} + 2\pi\,\gamma = 0\,, \qquad (2\text{-}10)$$

$$\therefore\ \mu_{M(island)} - \mu_{M(adatom)} = \mu^0_{M(island)} - \left(\mu^0_{M(adatom)} + kT\ln c_r^{eq}\right) = -\frac{\gamma\,\Omega}{r}, \qquad (2\text{-}11)$$

where c_r^{eq} is the equilibrium adatom density just outside an island of radius r. Equation (2-11) is also obtained from the two dimensional extension of Eq. (2-1). c_r^{eq} is equal to the equilibrium adatom density c_∞^{eq} just outside a straight step edge when the radius r of the island enlarged to infinity, therefore, the boundary condition is given by the following equation;

$$\mu^0_{M(island)} - \left(\mu^0_{M(adatom)} + kT\ln c_\infty^{eq}\right) = 0\,, \qquad (2\text{-}12)$$

From Eq. (2-11) and (2-12), one finds

$$kT \ln c_r^{eq} - kT \ln c_\infty^{eq} = \frac{\gamma \Omega}{r}, \tag{2-13}$$

$$\therefore c_r^{eq} = c_\infty^{eq} \exp\left(\frac{\gamma \Omega}{rkT}\right), \tag{2-14}$$

References

[1] M. Volmer and I. Estermann, Z. Phys. **7** (1921) 13.

[2] G. Neumann and G. M. Neumann, Surface Self-Diffusion of Metals, Diffusion Information Center, Ohio (1972).

[3] M. C. Tringides, in: Surface Diffusion: Atomistic and Collective Processes, edited by M. C. Tringides, Plenum Press, New York (1997) 1.

[4] E. W. Müller, Z. Phys. **131** (1951) 136.

[5] C. Herring, J. Appl. Phys., **21** (1950) 301.

[6] C. Herring, in: Structure and Properties of Solid Surfaces, edited by R. Gomer and C. S. Smith, Univ. Chicago Press, Chicago (1953) 5.

[7] N. A. Gjstein, in: Surfaces and Interfaces: Chemical and Physical Characteristics, edited by J. J. Burke, N. L. Reed and V. Weiss, Syracuse Univ. Press, Syracuse (1966) 271.

[8] D. J. Trevor and C. E. D. Chidsey, J. Vac. Sci. Technol. B, **9** (1991) 964.

[9] H. Honbo, S. Sugawara and K. Itaya, Anal. Chem., **62** (1990) 2424.

[10] H. Honbo and K. Itaya, J. Chim. Phys., **88** (1991) 1477.

[11] P. L. Mccarley and A. J. Bard, J. Phys. Chem., **96** (1992) 7410.

[12] N. Ikemiya, S. Miyaoka and S. Hara, Surf. Sci., **311** (1994) L641

[13] N. Ikemiya, S. Miyaoka and S. Hara, Surf. Sci., **327** (1994) 261

[14] N. Ikemiya, M. Nishide, S. Hara, Surf. Sci., **340** (1995) L965.

[15] D. R. Peale and B. H. Cooper, J. Vac. Sci. Technol. A, **10** (1992) 2210.

[16] B. H. Cooper, D. R. Peale, J. G. McLean, R. Phillips and E. Chason, in: Evolution of Surface and Thin Film Microstructures, edited by H. A. Atwater, E. Chason, M. H. Grabow and M. G. Lagally, MRS Symp. Proc., **280**, Mat. Res. Soc., Pittsburgh (1993) 37.

[17] K. Morgenstern, G. Rosenfeld and G. Comsa, Phys. Rev. Lett., **76** (1996) 2113.

[18] G. Rosenfeld, K. Morgenstern and G. Comsa, in: Surface Diffusion: Atomistic and Collective Processes, edited by M. C. Tringides, Plenum Press, New York (1997) 361.

[19] W. Theis, N. C. Bartelt and R. M. Tromp, Phys. Rev. Lett., **75** (1995) 3328.

[20] A. Ichimiya, Y. Tanaka and K. Ishiyama, Phys. Rev. Lett., **76** (1996) 4721.

[21] Y. Tanaka, K. Ishiyama and A. Ichimiya, Surf. Sci., **357-358** (1996) 840.

[22] A. Ichimiya, Y. Tanaka and K. Hayashi, Surf. Sci., **386** (1997) 182.

[23] A. Ichimiya, Y. Tanaka and K. Hayashi, Surf. Rev. Lett., **5** (1998) 821.

[24] A. Kraus, S. Hildebrandt, R. Kulla, G. Wilhelmi and H. Neddermeyer, Appl. Phys. A, **66** (1998) S953. Note that some part of the discussion is corrected in the literature [26]

[25] A. Ichimiya and K. Hayashi, J. Surf. Sci. Soc. Jpn., **20** (1999) 865.

[26] S. Hildebrandt, A. Kraus, R. Kulla and H. Neddermeyer, in: Proc. Workshop on Surface Science, Fundamental Electronics Research Instisute, Osaka Electro-Communication University, Osaka (2000) 1.

[27] J. Villain, Europhys. Lett., **2** (1986) 531.

[28] M. A. Dubson and G. Jeffers. Phys. Rev. B, **49** (1994).

[29] J. G. McLean, B. Krishnamachari, E. Chason, D. R. Peale, J. P.Sethna and B. H. Cooper, in: Surface Diffusion: Atomistic and Collective Processes, edited by M. C. Tringides, Plenum Press, New York (1997) 377.

[30] A. Natori, M. Murayama, D. Matsumoto and H. Yasunaga, Surf. Sci., **409** (1998) 160.

Chapter 3.

Decay of Holes Located on Ag(100) Surface in Contact with Aqueous Solution under the Control of Potential

I. Introduction

In the last chapter, I have investigated the decay of homogenous multi-layered islands atop of the terrace on Au (100) and Au(111) single crystals in 0.05 M H_2SO_4 aqueous solution under the control of potential at room temperature by *in-situ* EC-AFM, and discuss the influence of the applied potential and the orientation of substrate. Additionally, the island decay of silver seems to be also very interesting from the viewpoint of the influence of the material of the substrate upon the surface dynamics in electrolyte. However, I have not succeeded in building islands on silver substrate yet.

Scanning probe microscopy (SPM) can be utilized not only for the characterization of surfaces, but also for the nano-fabrication on surfaces. Ikemiya *et al.* has succeeded in fabricating a hole on Au(100) surface in 0.05 M H_2SO_4 aqueous solution under the control of potential at room temperature by an AFM cantilever and has estimated the self-diffusion coefficient (D_S) values on Au(100) from the observation of the decay of the hole [1]. In this chapter, I observe the decay of the hole, which is made on Ag(100) surface in 0.05 M H_2SO_4 aqueous solution under the control of potential at room temperature by an AFM cantilever, and the D_S values on Ag(100) are compared with those on Au(100).

II. Experimental

The Ag(100) samples were prepared from an Ag single crystal rod (12 mm diameter), which was grown by the Bridgman method. Orientation of the samples was verified within $\pm 1^\circ$ by Laue backscattering method. After mechanically polished, the samples were etched in a solution of 15 ml of ammonia solution, 5 ml of hydrogen peroxide solution and 80 ml of distilled

water for 1 minutes in order to remove the damaged layers by mechanical polishing. After being annealed at 700 K for 30 min in H_2 gas, silver was deposited onto Ag(100) substrate in 0.05 M H_2SO_4 + 10^{-3} M Ag_2SO_4 aqueous solution at 0.3 V for 30 minutes in order to make the surface atomically flat on a larger scale. The deposition rate of silver was about 3 monolayers per minute. Although the reference electrode actually used here was the Hg/Hg_2SO_4 electrode, all potential was referred to NHE in this chapter. The electrolytes used were prepared from H_2SO_4 (Wako, Superior), Ag_2SO_4(Wako) and MilliQ-water, and they were deaerated with Ar gas for more than 1 hour before each experiment.

The D_S values on Ag(100) were measured using the following procedure. By scanning continuously on a small area of the sample with the AFM tip in 0.05 M H_2SO_4 aqueous solution at 0.35 V for a few minutes, a small hole can be easily created. For making a hole, the force between the tip and the surface is in 10^{-7} N order, otherwise, for imaging, it is in the 10^{-9} N order. Subsequently, the potential was jumped to a different potential of interest for surface self-diffusion measurements in the double layer region (between –0.05 and 0.35 V) and the scan area was enlarged. The D_S values were calculated from successive AFM images that showed the refilling process of the hole.

III. Results and discussion

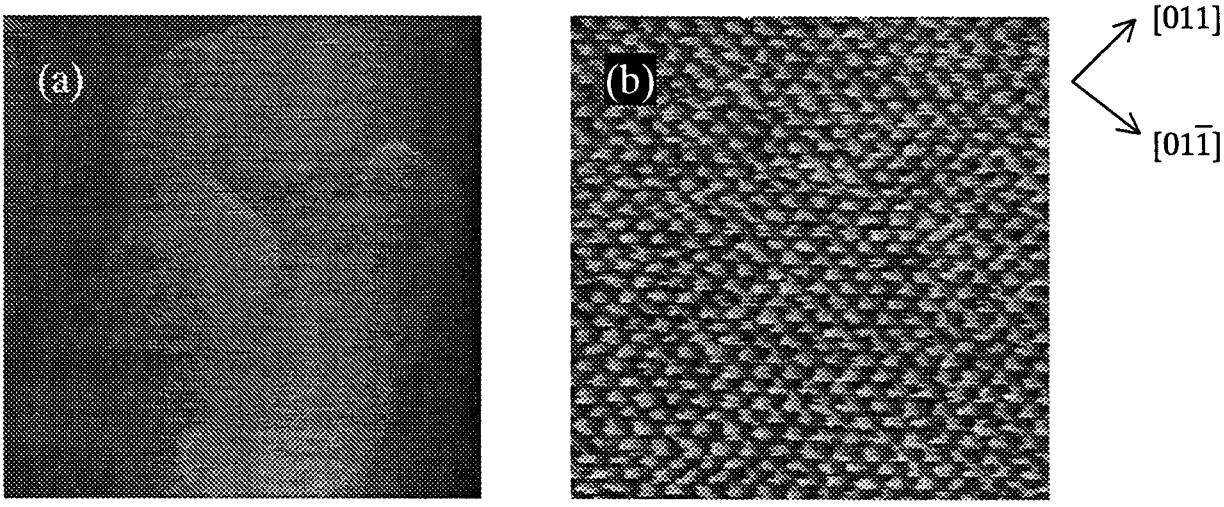

Figure 3-1 AFM images of Ag(100) surface obtained at 0.15 V in 0.05 M H_2SO_4 + 10^{-3} M Ag_2SO_4 aqueous solution after the deposition of silver for 30 minutes. (a) Large area image (700×700 nm, height mode image). (b) High resolution AFM image (8×8 nm), showing an unreconstructed Ag(100)-(1×1) structure.

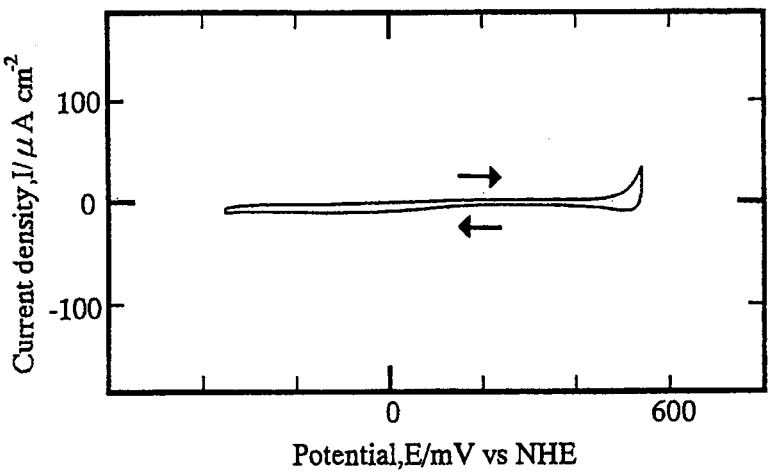

Figure 3-2 Cyclic Voltammogram for Ag(100) in 0.05 M H_2SO_4 aqueous solution between –0.35 and 0.55V with sweep rate of 50 mV/sec.

Figure 3-1(a) shows an AFM image (height mode) of Ag(100) surface at 0.15 V in 0.05 M H_2SO_4 + 10^{-3} M Ag_2SO_4 aqueous solution after the deposition of silver for 30 minutes. On the flat terrace of Ag(100) surface, an unreconstructed Ag(100)-(1 × 1) structure at 0.15 V was observed, as shown in Fig. 3-1(b).

Figure 3-2 shows a typical CV for Ag(100) in 0.05 M H_2SO_4 aqueous solution. The sweep potential was from –0.35 to 0.55 V and the scan rate was 50 mV/s. As can be seen from Fig. 3-2, the CV is characterized by a double-layer region between the anodic peak of Ag dissolution at 0.55 V and the cathodic peak of H_2 evolution at –0.35 V.

After making a hole on atomically flat Ag (100) surface, refilling process of the hole was observed at various potentials. Figure 3-3 shows a series of AFM images (height mode) of the refilling process at 0.25 V along with the cross section views. Figure 3-3(a) is an image taken immediately the hole was made. Usually, the depth of the hole was about 3 nm. Around the hole, a hill was observed. As shown in Figs. 3-3(b) and (c), the disappearance of the hole could be observed. Figure 3-4 shows a typical example for the relationship between the depth of the hole d on Ag(100) and time, obtained at 0.25 V. It was found that the depth of the hole decreases linearly with time in all experiments. Therefore, assuming that the hole is refilled by the random walk motions of Ag adatoms on terraces, the D_S values were calculated from the following equation,

$$D_S = L^2/2t_1, \qquad (3\text{-}1)$$

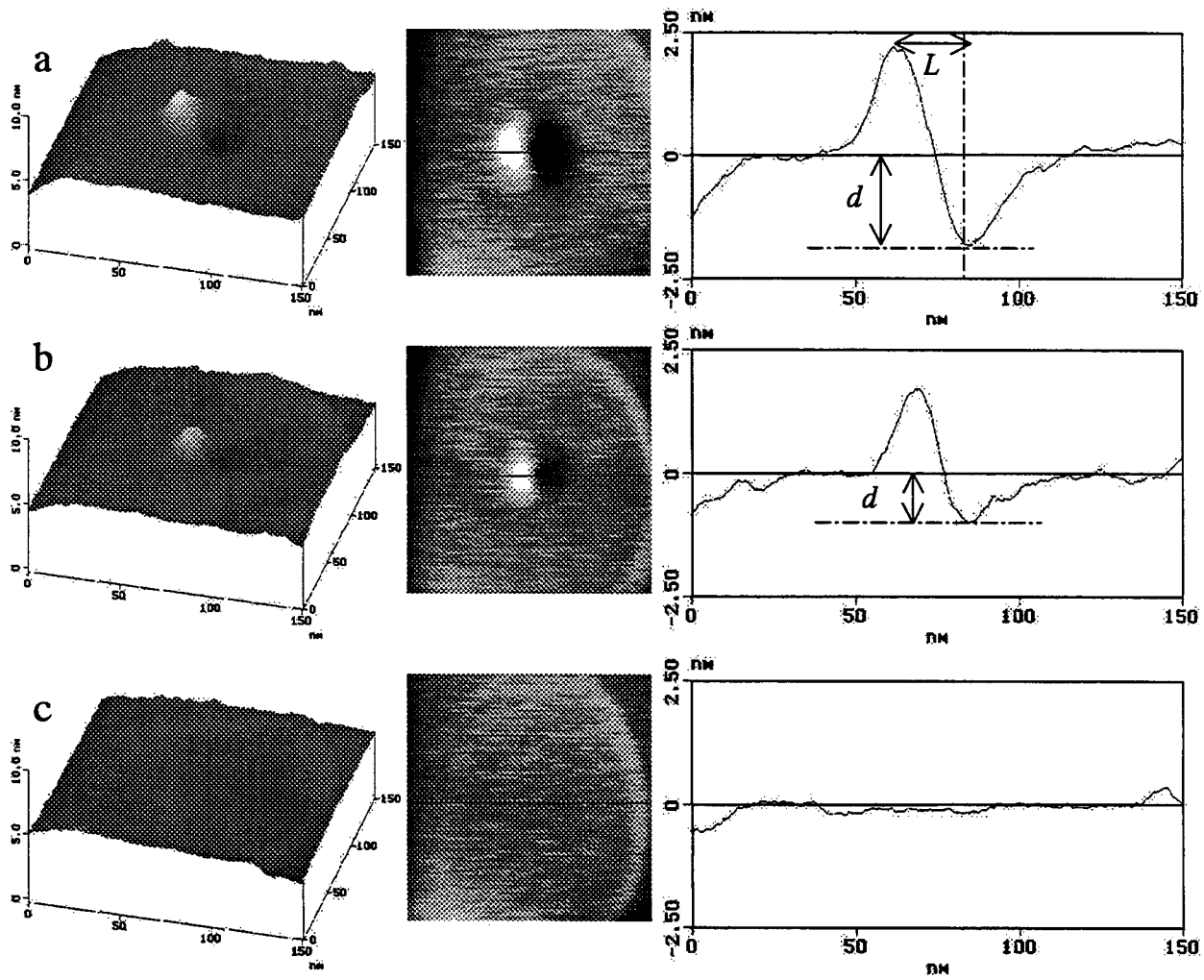

Figure 3-3 Series of AFM images (150×150 nm) together with the cross section views obtained at 0.25 V showing the refilling process of the hole created on the terrace. Image (a) was taken immediately after the hole was made. The images (b) and (c) were obtained 50 and 134 sec. after taken image (a), respectively.

where L is the horizontal distance between the top of the hill and the bottom of the hole, and t_1 is the average refilling time per atomic layer.

Figure 3-5 shows the relationship between D_S on Ag(100) and the applied electrode potential E. For comparison, the D_S values observed on Au(100) [1] are also plotted. The D_S values on Ag and Au in vacuum extrapolated from the following equation [2],

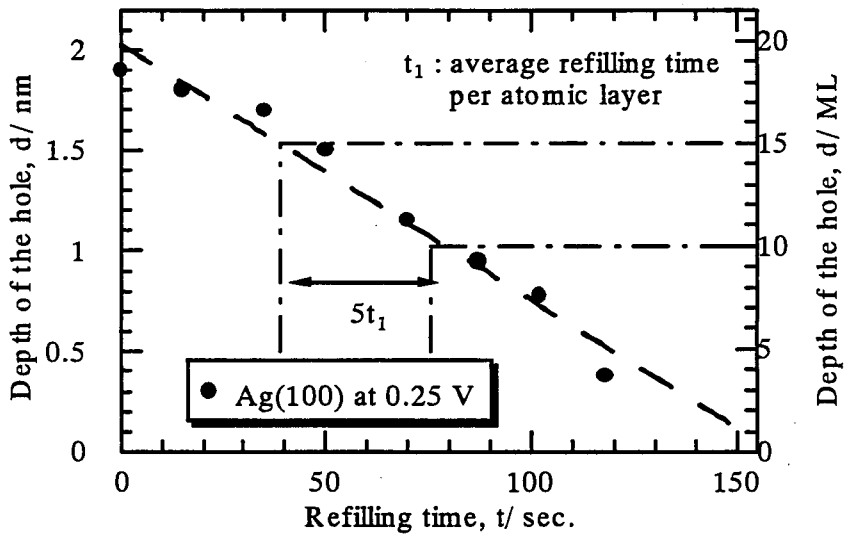

Figure 3-4 Typical example for the relationship between the depth of the hole on Ag(100) and time, obtained at 0.25 V.

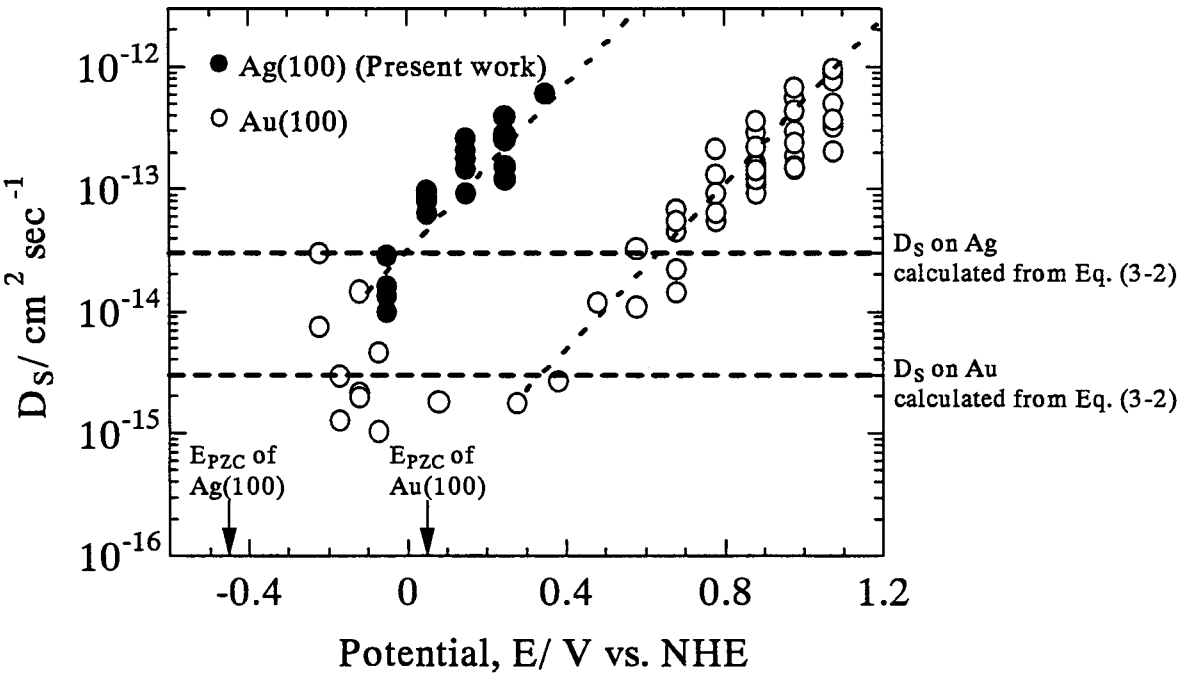

Figure 3-5 Relationship between the surface self-diffusion coefficient D_S and the applied electrode potential E. The dots are the experimental D_S values of Ag(100) and Au(100) and the dotted lines are the D_S values of Au(100) and Ag(100) calculated from Eq. 3-4, where the constant $\alpha\ \beta$ is assumed 0.4. The broken lines are the extrapolated D_S values of Ag and Au under vapor phase, reported by Gjostein [2].

$$D_S = D_{S0} \exp\left(\frac{-Q_S}{RT}\right) [\text{cm}^2\,\text{sec}^{-1}], \tag{3-2}$$

at $D_{S0} = 0.014\,[\text{cm}^2\,\text{sec}^{-1}]$, $Q_S = 13T_m$ [cal mole^{-1}] $= 54.6T_m$ [J mole^{-1}],

are also shown in Fig. 3-5, where Q_S is the activation energy for surface self-diffusion, D_{S0} is a pre-exponential factor, T_m is the melting temperature (T_m = 1234 K for Ag, T_m = 1336 K for Au) and T is the experimental temperature (T = 298 K). The volume diffusion constant (D_V) can be ignored, because it is several orders of magnitude smaller than D_S [3]. In the case of Au(100), the minimum value of D_S in 0.05 M H_2SO_4 aqueous solution was located at E_{PZC} of Au(100) and it agrees well with that extrapolated from Eq. (3-2). In the case of Ag(100), however, the extrapolated D_S value at –0.45 V, which is the E_{PZC} of Ag(100) in 0.01 M Na_2SO_4 aqueous solution [4], is much smaller than that calculated from Eq. (3-2). It should be discussed whether D_{S0} and Q_S in Eq. (3-2) are valid or not for Ag(100), because on one hand, Eq. (3-2) was derived from experimental values at temperatures more than 700 K and on the other hand, the D_S values of Ag derived from Eq. (3-2) were about a hundred times larger than the experimental ones even at 880 K [2]. Another question arises from whether the E_{PZC} of –0.45 V in 0.01 M

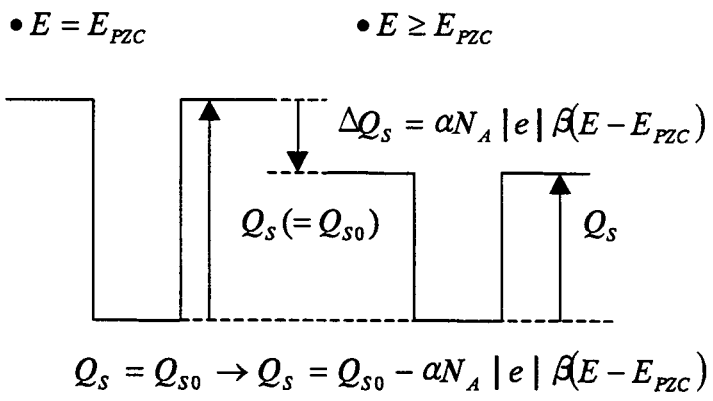

Figure 3-6 Schematic illustrations of the activation energy ΔQ_S of surface diffusion of Ag (or Au) adatom under the presence of applied potential (E), if $E \geq E_{PZC}$. Q_{S0} is the activation energy of surface diffusion at $E = E_{PZC}$ and ΔQ_S is the reduction in the activation energy of surface diffusion at $E \geq E_{PZC}$ in comparison with at $E = E_{PZC}$.

Na_2SO_4 aqueous solution can be used or not for the experiments performed in 0.05 M H_2SO_4 aqueous solution.

From Fig. 3-5, it can also be seen that the D_S of Ag(100) increased exponentially with potential within the range from –0.05 to 0.35 V. The schematic diagram for the surface self-diffusion process of Ag(100) and Au(100) under the presence of applied potential E, shown in Fig. 3-6, is used for deriving the D_S-E relationship. The Q_{S0} is the activation energy of surface diffusion when the applied potential is E_{PZC} and is equal to the Q_S derived from Eq. (3-2). At $E \geq E_{PZC}$, the reduction in the activation energy for surface diffusion (ΔQ_S) can be obtained as

$$\Delta Q_S = \int q^M dV = \int CV dV = \frac{CV^2}{2} = \frac{q^M V}{2} = \frac{\alpha N_A |e| \beta (E - E_{PZC})}{2}, \qquad (3\text{-}3)$$

where $q^M (= CV = \alpha N_A |e|)$ is the surface excess charge, $V(= \beta(E - E_{PZC}))$ is the applied voltage between the inner Helmholtz layer and the surface, α and β are constants (absolute numbers), N_A is Avogadro's constant, and $|e|$ is the charge of an electron. Taking into account the consideration mentioned above,

$$D_S = D_{S0} \exp\left(\frac{-Q_S}{RT}\right) = D_{S0} \exp\left(\frac{-Q_{S0} + \frac{\alpha \beta N_A |e| (E - E_{PZC})}{2}}{RT}\right), \qquad (3\text{-}4)$$

$$\ln D_S = \left(\frac{\alpha \beta N_A |e|}{2RT}\right) E + \left(\ln D_{S0} - \frac{Q_{S0} + \frac{\alpha \beta N_A |e| E_{PZC}}{2}}{RT}\right), \qquad (3\text{-}5)$$

are derived from Eqs. (3-2) and (3-3). Equations (3-4) and (3-5) proposed by us take into consideration the effect of the applied potential on the surface self-diffusion. The dotted lines in Fig. 3-5 are the D_S of Au(100) and Ag(100) calculated from Eq. (3-4). The Q_S of Ag(100) was modified in Eq. (3-4) in order to fit the D_S value at $E = E_{PZC}$ predicted from experimental values with that extrapolated from Eq. (3-2). If $E_1 \approx E_2 >> E_{PZC}$ and if it is assumed that α and β at $E = E_1$ are nearly equal to those at $E = E_2$,

$$\ln D_S^{E=E_1} - \ln D_S^{E=E_2} = \frac{\alpha \beta N_A |e|}{2RT}(E_1 - E_2), \qquad (3\text{-}6)$$

can be obtained from Eq. (3-5). From Eq. (3-6) and D_S-E relationship, $\alpha\beta$ values can be

estimated. The value of 0.4 for $\alpha\beta$ of both Ag(100) and Au(100) at $E >> E_{PZC}$ was obtained from experimental values plotted in Fig. 3-5.

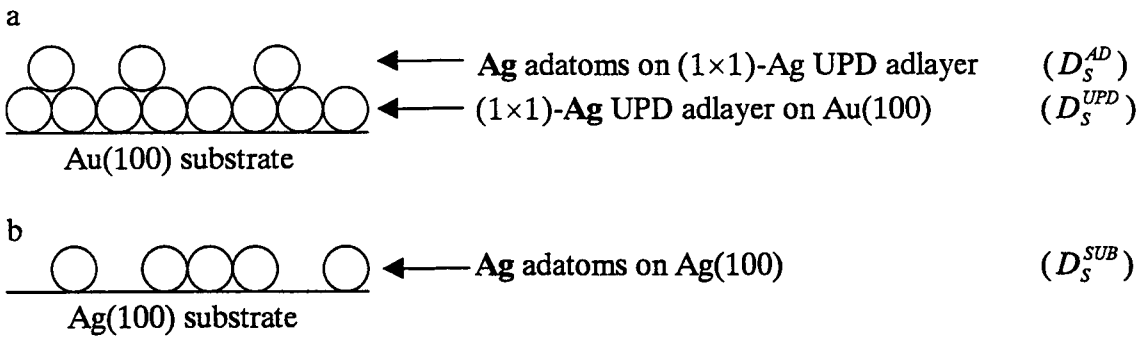

Figure 3-7 Schematic illustrations for (a) the diffusion of Ag on Au(100) and (b) the self- diffusion on Ag(100).

From Fig. 3-5, it was clearly seen that the D_S values on Ag(100) were about a hundred times larger than those on Au(100) 0.15 to 0.35 V. In the previous work [5], it was found that Ag films were formed on (1 x 1)-Ag UPD adlayer on Au(100) in 0.05 M H_2SO_4 + 10^{-3} M Ag_2SO_4 aqueous solution by an ideal layer-by-layer growth mode even at a high deposition rate ($\leq$7.2 ML min^{-1}) and the flatness of Ag films was improved as the deposition proceeded. Figure 3-7 shows the schematic diagram for the diffusion of Ag on Au(100) and the self- diffusion on Ag(100). Because adatoms were mainly attracted by the neighbors atoms, the D_S values of Ag adatoms on (1 x 1)-Ag UPD adlayer on Au(100) ($= D_S^{AD}$) must be similar to that on Ag(100) ($= D_S^{SUB}$). On the other hand, the D_S values of UPD Ag atoms on Au(100) ($= D_S^{UPD}$) must be smaller than D_S^{SUB}, because the UPD atoms were attracted by Au(100) surface atoms. From the considerations mentioned above, D_S^{AD} must be larger than D_S^{UPD}, i.e.:

$$D_S^{AD} \cong D_S^{SUB} > D_S^{UPD}, \tag{3-7}$$

therefore, the Ag adatoms can diffuse without too much moving of the Ag UPD layer.

IV. Conclusion

In this chapter, the decay of holes made by an AFM cantilever on Ag(100) surface was investigated by in-situ EC-AFM in 0.05 M H_2SO_4 aqueous solution under the control of potential

at room temperature. The D_S values were estimated from the EC-AFM observation of the decay and they were compared with those on Au(100) in the same solution. It is found that the D_S values of both Ag(100) and Au(100) increase exponentially with the applied potential. It is also found that the D_S values on Ag(100) were about a hundred times larger than those on Au(100) within the potential range from 0.15 to 0.35 V. From these D_S-E relationships, it is concluded that the activation energy of surface diffusion in aqueous solution decreases when the surface excess charge at metal/electrolyte interface increases.

References

[1] N. Ikemiya, M. Nishide and S. Hara, Surf. Sci. **340** (1995) L965.

[2] N. A. Gjstein, in: Surfaces and Interfaces: Chemical and Physical Characteristics, edited by J. J. Burke, N. L. Reed and V. Weiss, Syracuse Univ. Press, Syracuse (1966) 271.

[3] H. Gobel and P. V. Blanckenhagen, Surf. Sci. **331** (1995) 885.

[4] T. Vitanov and A. Popov, Dokl. Akad. Nauk. S.S.S.R. **226** (1976) 373.

[5] N. Ikemiya, K. Yamada and S. Hara, J. Vac. Sci. Technol. B **14** (1996) 253.

Chapter 4.

Initial Stage of Adsorption of Inhibitor on Copper Single Crystals in Aqueous Solution

I. Introduction

Benzotriazole ($C_6H_4N_3H$, BTAH), whose structural formula is shown in Figure 4-1, is known as a corrosion inhibitor for copper and copper alloys. There are some reports for the character of the BTAH films [1-12], however, the structure of the BTAH films still comes up for the discussion and it doesn't understand clearly. Especially, there is a little information about adsorbed structures of BTAH molecules on Cu single crystal. In ultrahigh vacuum (UHV), Cho *et. al* reported the ex-situ STM images of BTAH adsorbed on Cu(110) [1,2] and Walsh *et. al* observed the molecular orientation using near-edge extended X-ray absorption fine structure (NEXAFS) measurement [3]. Behm *et. al* reported currently the *in-situ* STM and FT-IR investigations of BTAH adsorbed on Cu(100) in sulfuric or hydrochloric acid aqueous solution [4,5]. However, more information is required to clarify the role of adsorbed BTAH as the inhibitor on Cu surface. In this chapter, I investigated adsorbed BTAH films on Cu(110), Cu(100) and Cu(111) single crystals in 0.1 M $HClO_4$ aqueous solution taken by *in-situ* EC- AFM, combined with CV and anodic polarization measurements.

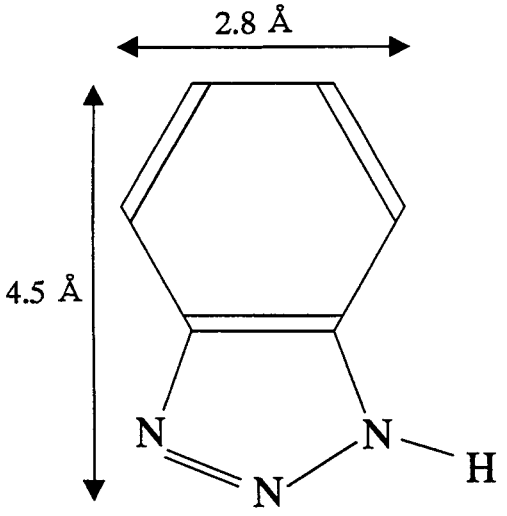

Figure 4-1 Structural formula of Benzotriazole (BTAH)

II. Experimental

Cu(110), Cu(100) and Cu(111) samples were prepared from a Cu single crystal rod (Furuuchi Chemical). Orientation of the samples was verified within $\pm 1^\circ$ by Laue

backscattering method. After mechanically polished, the samples were electropolished in 30% nital (30 volume % nitric acid + 70 volume % methanol) at 240 K for 5 minutes in order to remove the damaged layers by mechanical polishing. Only Cu(111) samples were annealed at 700 K for 30 minutes in H_2 gas before introducing into the EC-AFM, which was described in chapter 2.

In order to compare the corrosion resistance of BTAH films adsorbed on Cu single crystals, I have also measured anodic polarization curves of Cu single crystals in aqueous solution with BTAH. The procedures before the anodic polarization measurement starts are as follows. After introducing a sample into a solution without BTAH, the applied potential of the sample was kept at –1.2 V for 3 minutes in order to expose a clean and bare surface. Then, a suitable amount of BTAH was stirred into the solution, followed by keeping the potential at a rest potential of the sample for 5 minutes in order to form an adsorbed BTAH film on the sample. After these procedures, the scan for anodic polarization measurement started in the positive direction from the rest potential, and a "breakdown potential" was defined as a potential at which an anodic current density exceeds 1 mA cm^{-2} in order to estimate the corrosion resistance of the film. The measurements under each condition have been performed more than three times. Although the reference electrode actually used here was the Hg/Hg_2SO_4 electrode, all potential was referred to NHE in this chapter. The electrolytes used were prepared from $HClO_4$ (Wako, Superior), H_2SO_4 (Wako, Superior), 1,2,3-BTA (Wako) and MilliQ-water, and they were deaerated with Ar gas for more than 1 hour before each experiment.

III. Results and Discussion

III-1. Cyclic Voltammetry

Figure 4-2 shows CVs for Cu(110) in 0.1 M $HClO_4$ aqueous solution without BTAH (a) and with 10^{-3} M BTAH (b) with sweep rate of 50 mV sec^{-1}. The CV without BTAH, shown in Fig. 4-2(a), is characterized by a double-layer region from 0.20 V for the anodic peak of Cu dissolution to –0.45 V for the cathodic peak of H_2 evolution. The anodic and the cathodic peaks are also observed for the solution with 10^{-3} M BTAH (Fig. 4-2(b)), but the height decreases in comparison with that for no addition of BTAH (Fig. 4-2(a)). CVs for Cu(100) is quite similar to those for Cu(110).

Figure 4-3 shows CVs for Cu(111) in 0.1 M $HClO_4$ aqueous solution without BTAH (a) and with 10^{-3} M BTAH (b) with sweep rate of 50 mV sec^{-1}. The CV has a clear cathodic peak at

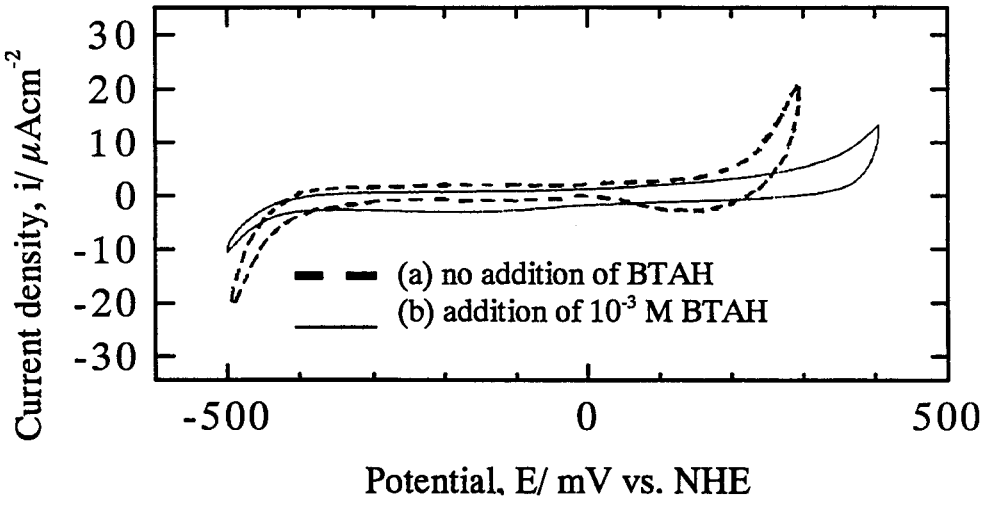

Figure 4-2 Cyclic voltammograms for Cu(110) in 0.1 M $HClO_4$ aqueous solution without BTAH (a) and with 10^{-3} M BTAH (b) with sweep rate of 50 mV sec^{-1}.

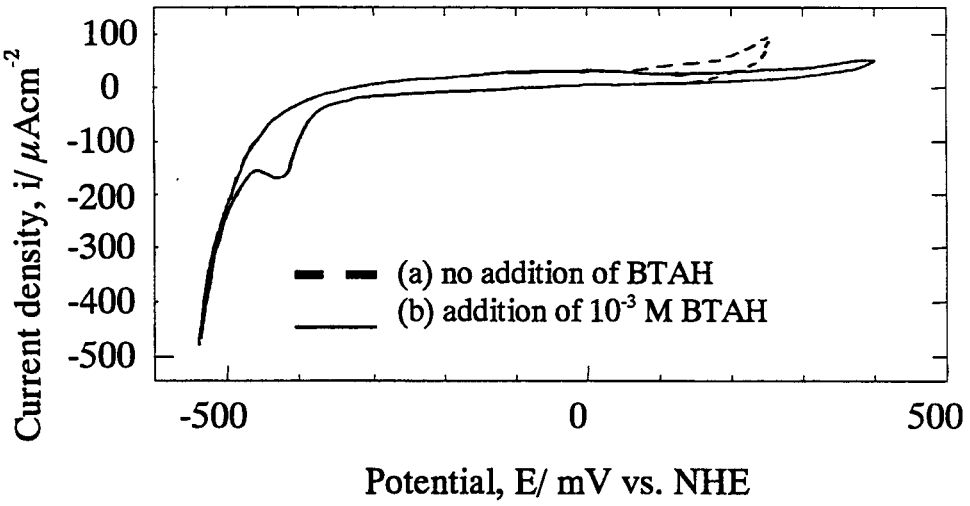

Figure 4-3 Cyclic voltammograms for Cu(111) in 0.1 M $HClO_4$ aqueous solution without BTAH (a) and with 10^{-3} M BTAH (b) with sweep rate of 50 mV sec^{-1}.

–0.4 V and a small anodic peak at 0 V, which are considered to be caused by the specific adsorption and desorption of perchloric acid anions, in addition to the peaks of Cu dissolution and H_2 evolution, which are also observed for Cu(110) and Cu(100). It is interesting that the height of the H_2 evolution peak for the solution with 10^{-3} M BTAH does not decrease in comparison with that for no addition of BTAH in the case of Cu(111). It is considered that the BTAH molecules can not adsorb on Cu(111) in cathodic region, as also discussed in the next paragraph.

III-2. *In-situ* EC-AFM Observation

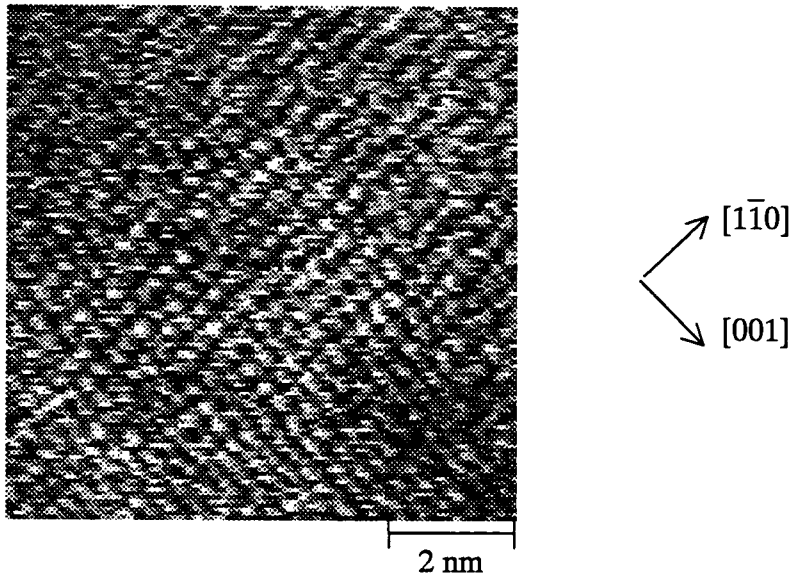

Figure 4-4 AFM image of Cu(110) in 0.1 M $HClO_4$ solution without BTAH at –0.4 V.

Figure 4-4 shows an AFM image for a bare Cu(110) surface, whose nearest and next nearest distances are 0.36 nm and 0.26 nm, observed by *in-situ* AFM in 0.1 M $HClO_4$ aqueous solution without BTAH at –0.4 V after keeping at –0.45 V for a few minutes in order to remove the oxide of copper. The structure fitted well for the unreconstructed Cu(110) surface, is observed at the double layer region between –0.4 V to 0.2 V.

In 0.1 M $HClO_4$ aqueous solution with 10^{-3} M BTAH, Cu(110)-(1×1) structure was also observed at the potential between –0.25 V and –0.15 V. At the potential from –0.5 to –0.25 V and from –0.15 to 0.4 V, two structures, which are different from Cu(110)-(1×1) structure, were observed as shown in Fig. 4-5(a) and Fig. 4-6(a),. The AFM image taken at 0.4 V as shown in Fig. 4-5(a), is characterized by two arrows of periodical protrusions with 0.62 nm and 0.72 nm. Figure 4-5(b) indicates a schematic figure of the structure shown in Fig.4-5(a). This structure corresponds to c(2×4) structure, is the same as observed in UHV [1,2] and it is shown in Fig. 4-5(a) with white lines.

As shown in Fig. 4-6(a), I also detected a structure at 0.2 V with the nearest and the next nearest distances of 0.53 nm and 0.72 nm, respectively. This c(2×3) structure is shown schematically in Fig. 4-6(b). The c(2×3) lattice is also shown in Fig. 4-6(a) with white lines. This structure was not observed in UHV.

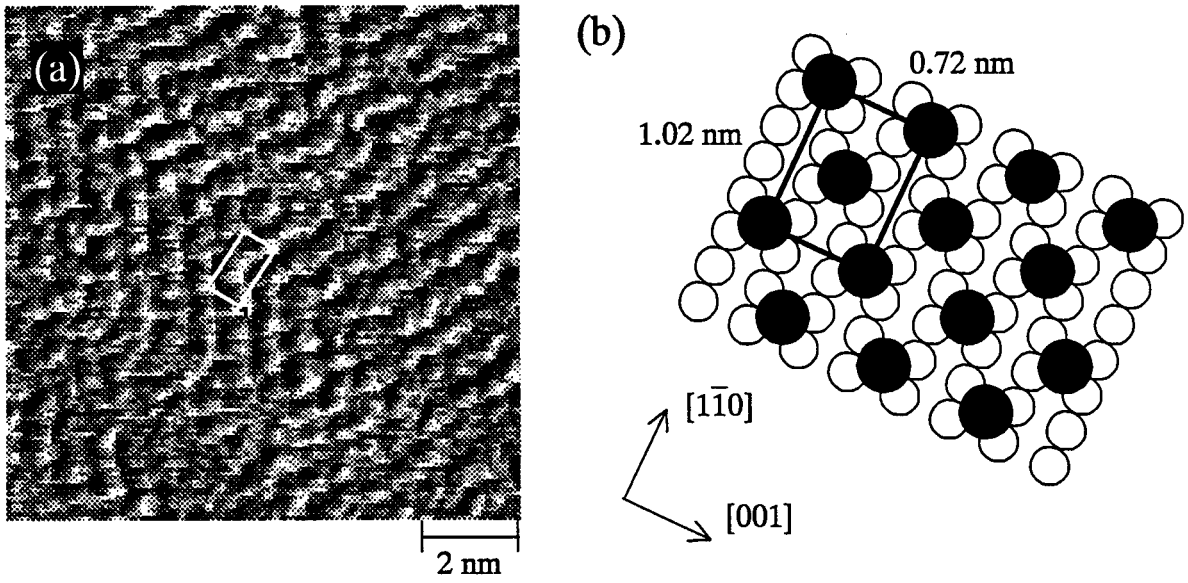

Figure 4-5 (a) AFM image of Cu(110) in 0.1 M $HClO_4$ aqueous solution with 10^{-3} M BTAH at 0.4 V and (b) schematic figure of the c(2×4) structure.

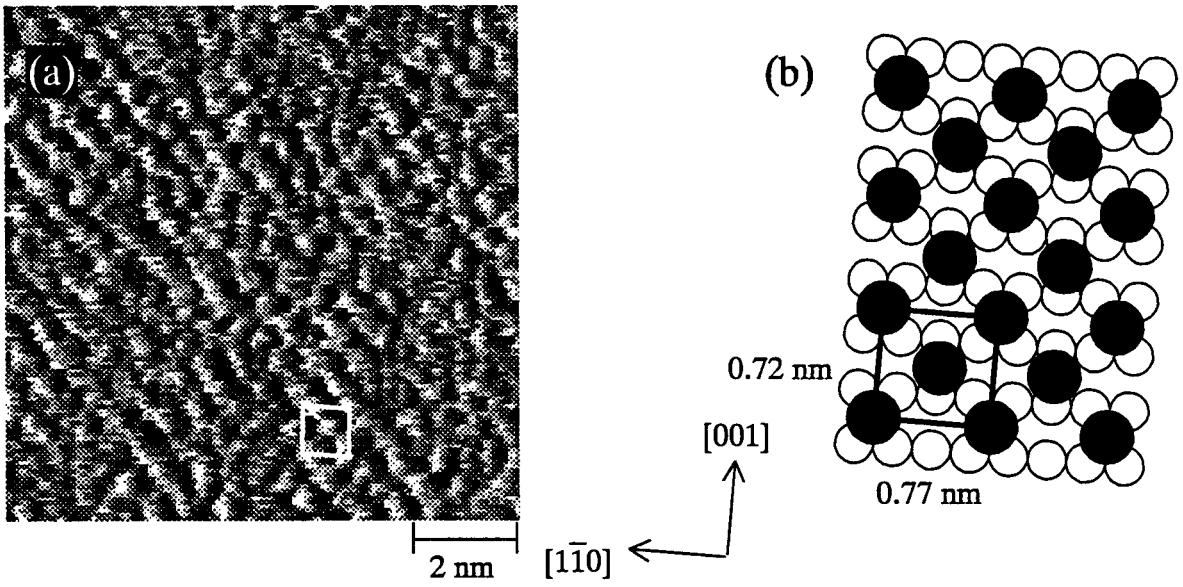

Figure 4-6 (a) AFM image of Cu(110) in 0.1 M $HClO_4$ aqueous solution with 10^{-3} M BTAH at 0.2 V and (b) schematic figure of the c(2×3) structure.

In comparison with Figs. 4-5 and 4-6, the periodicity for [001] direction of adsorbed BTAH molecules is common, but that for [1$\bar{1}$0] is different. In the case of Cu(100) in sulfuric or

hydrochloric acid solution, the periodicity for one direction is common and that for another direction is different, too [4,5].

Table 4-1 Observed structures on Cu(110), Cu(100) and Cu(111) single crystals in 0.1 M $HClO_4$ aqueous solution without BTAH or with 10^{-3} M BTAH by in-situ EC-AFM

orientation	solution	Potential, E/mV vs. NHE (-500 … 0 … 500)					
Cu(110)	without BTAH	H	Cu(110)-(1x1)			D	
	with 1mM BTAH	H	BTA-c(2×3)	Cu(110)-(1x1)	BTA-c(2×3) BTA-c(2×4)	※	D
Cu(100)	without BTAH	H	Cu(100)-(1x1)	O^{2-} or OH^- -($\sqrt{2}\times\sqrt{2}$)R45°		D	
	with 1mM BTAH	H	BTA-($\sqrt{5}\times\sqrt{13}$), BTA-($\sqrt{5}\times3\sqrt{2}$)			※	D
Cu(111)	without BTAH	H	Cu(111)-(1x1)	ClO_4^--($\sqrt{3}\times\sqrt{3}$)R30°		D	
	with 1mM BTAH	H	Cu(111)-(1x1)	ClO_4^--($\sqrt{3}\times\sqrt{3}$)R30°?		※	D

H: H_2 evolution D: Cu dissolution ※: Super lattice structure was gradually disappeared

Table 4-1 shows observed structures on Cu(110), Cu(100) and Cu(111) single crystals in 0.1 M $HClO_4$ aqueous solution without BTAH or with 10^{-3} M BTAH by in-situ EC-AFM in the present work. The fact that Cu(111)-(1×1) structure is observed in 0.1 M $HClO_4$ aqueous solution with 10^{-3} M BTAH from –0.45 to –0.2 V agrees with the CV measurements.

III-3. Anodic Polarization Measurement

The "breakdown potentials", the anodic potentials at 1 mA cm^{-2}, of the BTAH films adsorbed on Cu(100), Cu(110) and Cu(111) in 0.1 M $HClO_4$ aqueous solution with 10^{-3} M BTAH are shown in Fig. 4-7. For comparison, that in 0.05 M H_2SO_4 aqueous solution with 10^{-3} M BTAH is also plotted in Fig. 4-7. The influence of orientation upon the breakdown potentials is not clear, whereas the breakdown potentials in perchloric acid solution are more positive than those in sulfuric acid solution. From this fact and another two experimental ones as shown below, it is considered that the hindrance of sulfuric anions, which adsorbed on copper surface more strongly than perchloric ones, to the arrangement of BTAH molecules adsorbed on copper makes

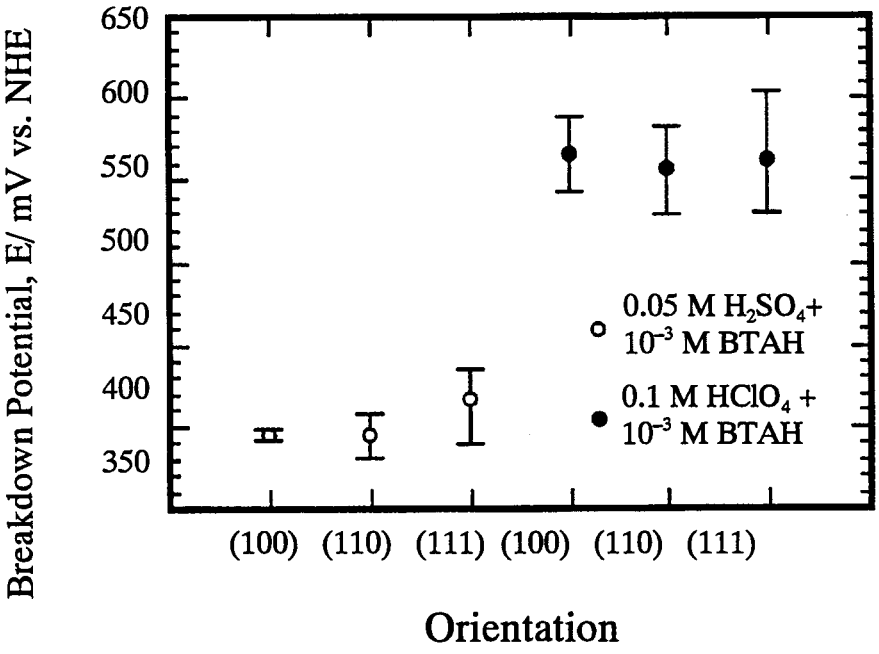

Figure 4-7 Breakdown potentials of the films adsorbed on Cu(100), Cu(110), Cu(111) in 0.1 M $HClO_4$ solution with 10^{-3} M BTAH and in 0.05 M H_2SO_4 solution with 10^{-3} M BTAH. The open and closed circles indicate the mean values of the breakdown potentials. The error bars indicate the scatter in measured values.

the BTAH films have more defects.

1. In 0.1 M $HClO_4$ aqueous solution with 10^{-3} M BTAH, I observed various ordered structures, as shown in Table 4-1, whereas no ordered structure was observed in 0.05 M H_2SO_4 aqueous solution with 10^{-3} M BTAH by *in-situ* EC-AFM.
2. After these anodic polarization measurements, only a few pits were observed in perchloric acid solution, while many pits were observed in sulfuric acid solution by the observation with naked eyes.

IV. Conclusion

In this chapter, I investigated Cu(110), Cu(100) and Cu(111) surface in 0.1 M $HClO_4$ aqueous solution with or without 10^{-3} M BTAH by *in-situ* EC-AFM and electrochemical methods. From the CVs, I observed that both reactions, Cu dissolution at 0.25 V and H_2 evolution at –0.5 V, were suppressed by the addition of BTAH, except the H_2 evolution on Cu(111). By in-situ EC-AFM, I have observed various ordered structures as shown in Table 4-1. From the anodic

polarization measurements, it is found that the breakdown potentials of the BTAH films adsorbed on Cu single crystals in perchloric acid solution are more positive than those in sulfuric acid solution.

References

[1] K. Cho, J. Kishimoto, T. Hashizume and T. Sakurai, Jpn. J. Appl. Phys., **33** (1994) L125.

[2] K. Cho, J. Kishimoto, T. Hashizume, H. W. Pickering and T. Sakurai, Appl. Surf. Sci., **87/88** (1995) 380.

[3] J. F. Walsh, H. S. Dhariwal, A. Gutiérrez-Sosa, P. Finetti, C. A. Muryn, N. B. Brookes, R. J. Oldman and G. Thornton, Surf. Sci., **415** (1998) 423.

[4] M. R. Vogt, W. Polewska, O. M. Magnussen and R. J. Behm, J. Electrochem. Soc., **144**(5), (1997) L113.

[5] M. R. Vogt, A. Lachenwitzer, O. M. Magnussen and R. J. Behm, Surf. Sci., **339** (1998) 49.

[6] G. D. Zhow, H. Shao, and B. H. Loo, J. Electrochem. Soc., **421**(1-2) (1997) 129.

[7] L. Tommesani, G. Brunoro, A. Frignani, C. Monticelli and C. M. Dal, Corro. Sci., **39**(7) (1997) 1221.

[8] M. A. Pawz, J. H. Zagal, O. Bustos, M. J. Aguirre, P. Skeldon and G. E. Thompson, Electrochim. Acta, **42**(23-24) (1997) 3453.

[9] D. Tromans, J. Electrochem. Soc, **145**(3) (1998) L42.

[10] D. Papapanayiotou, H. Deligianni and R. C. Alkire, J. Electrochem. Soc., **145**(9) (1998) 3016.

[11] H. C. Jin, C. L. Zhi, C. Shu, H. N. Li and Z. Y. Shou, Electrochim. Acta, **43**(3-4) (1998) 265.

[12] H. M. Metikos, R. Babic and A. Marinovic, J. Electrochem. Soc., **145**(12) (1998) 4045.

Chapter 5.

Initial Stage of Anodic Oxidation of Iron Single Crystals in Aqueous Solution

I. Introduction

The characteristics of iron in aqueous solution are very interesting in order to study the corrosion processes because of its theoretical and industrial importance. The passive films formed on iron in aqueous solution have been investigated with ex situ and *in-situ* techniques, e. g. X-ray photoelectron spectroscopy (XPS) [1-5], Auger electron spectroscopy (AES) [6-9], Mössbauer spectroscopy [1,10-13], secondary ion mass spectroscopy (SIMS) [8,14,15] , ellipsometry [16-21], surface enhanced Raman spectroscopy (SERS) [22-27], light reflectance spectroscopy [28,29], X-ray absorption near-edge structure (XANES) study [30] and scanning electrochemical microscopy (SECM) [31], but more information is required for better understanding about the behavior of iron in aqueous solution.

Scanning tunneling microscopy (STM) and atomic force microscopy (AFM) are powerful techniques for *in-situ* studies of surfaces in electrochemical environment. Especially, the STM and AFM investigation on an atomic scale with the electrochemical oxidation processes of a well-defined electrode surface of base metals, such as copper [32,33], nickel [34-36] and cobalt [37], is intriguing because it gives information about the epitaxial relationship between anodically formed oxide layer and substrate.

A few STM and AFM observations about the oxidation and corrosion of iron in aqueous solution were performed previously. *In-situ* electrochemical topological, not atomic resolution, STM and AFM studies were carried out in borate [38,39], citrate [40] and alkaline[41,42] solution. M. P. Ryan *et al.* [43] succeeded in atomically resolved STM observation upon the anodic oxide layer formed on the sputtered thin iron film in borate solution. However, atomic resolution images of unoxidized bare Fe surfaces were not obtained both in air and in solution because of the stability of oxide layer. Therefore, it was not clarified how the orientation of the anodically formed oxide film is related to that of iron substrate.

In the present paper, I show *in-situ* atomic resolution AFM images of a bare Fe(110)

single crystal and an anodically formed oxide layer on Fe(110) in 0.05 M Na_2SO_4 and 0.01 M NaOH aqueous solution under the control of potential. From these images, I discuss an epitaxial relationship between the anodically formed oxide layer and the iron substrate.

II. Experimental

Fe(110) samples were prepared from a Fe single crystal rod (99.9%, Monocrystal). Orientation of the samples was verified within $\pm 1^\circ$ by Laue backscattering method. After mechanically polished, the samples were etched in 3 % HF-97 % H_2O_2 solution for 10 minutes in order to remove the damaged layers. Although the reference electrode actually used here was the Hg/Hg_2SO_4 electrode, all potential was referred to NHE in this chapter. The electrolytes used were prepared from Na_2SO_4 (Wako) and MilliQ-water, and they were deaerated with Ar gas for more than 1 hour before each experiment.

III. Results and Discussion

Figure 5-1 indicates a typical CV for Fe(110) in 0.05 M Na_2SO_4 aqueous solution from –1.25 V to –0.05 V with sweep rate of 50 mV sec^{-1}. In the positive scan, there is an oxidation peak at –0.8 V (A_1), followed by the active region (A_2). This positive scan practically agrees with the anodic sweep voltammogram in neutral solution reported [44]. Reversing the potential toward negative at –0.05 V, there is a cathodic peak at –0.75 V (C_1), which is the reduction of the peaks (A_1, A_2) and is followed by hydrogen evolution region (C_2). The peak (A_1) is considered to be due to one monolayer formation of $Fe(OH)_2(0001)$ film on Fe(110) substrate according to the discussion below.

After setting the sample in EC-AFM, I tried to remove the effect of the oxide layer formed in air. First, I keep the potential at –1.85 V, where the unoxidized iron is stable according to the Pourbaix diagram [45], for 30 minutes, however, I didn't succeed in the exposure of any well-ordered structures. As the next trial, I tried to scan the surface by the AFM cantilever continuously for 10 minutes while keeping the potential at –1.85 V and succeed in the observation of an well-ordered structure. Figure 5-2(a) indicates an *in-situ* EC-AFM image taken at –1.25 V in 0.05 M Na_2SO_4 aqueous solution after the procedure described above and then stepping the potential from –1.85 V to –1.25 V because too high current density caused by hydrogen evolution reaction prevent us from obtaining a good AFM image. In the filtered image (Fig. 5-2(b)) of image (a), we can recognize the spots which have two-fold symmetry with

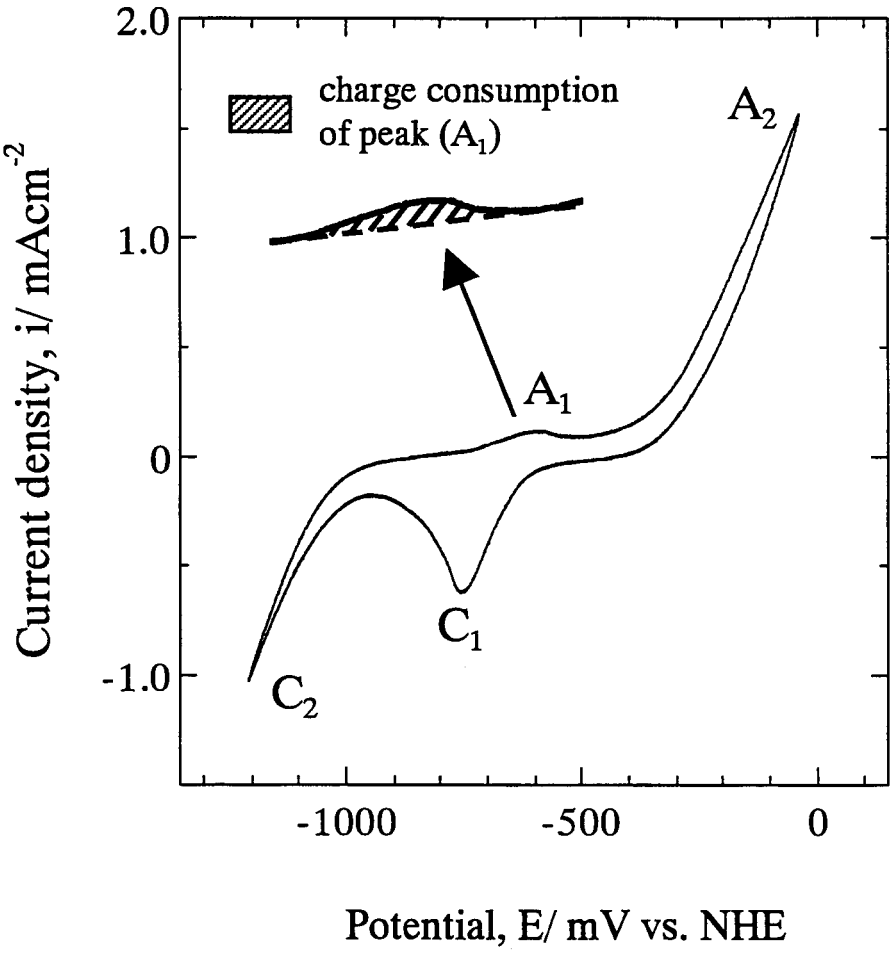

Figure 5-1 Cyclic voltammogram for Fe(110) electrode in 0.05 M Na_2SO_4 aqueous solution from –1.25 V to –0.05 V with sweep rate of 50 mV sec^{-1}.

interatomic distance of 0.29 nm and 0.40 nm. It corresponds well to a bare and unreconstructed Fe(110)-(1 × 1) structure as shown schematically in Fig. 5-2(c). This is the first *in-situ* EC-AFM image with atomic resolution of unpassivated iron electrodes in aqueous solution.

After observing the structure as shown in Figs. 5-2, the new well-ordered structure, as Fig. 5-3(a) shows, was exposed by only our stepping the potential from –1.25 V to –0.55 V, which is more positive than peak (A_1). In the filtered image (Fig. 5-3(b)) of image (a), we can recognize the spots which have three-fold symmetry with interatomic distance of 0.33 nm. This superlattice corresponds to the protuberances by OH groups or Fe atoms on unreconstructed $Fe(OH)_2$(0001)-(1 × 1) (Fig. 5-4(a)), since the bulk structure of $Fe(OH)_2$ is known as shown in Fig. 5-4(b). On one hand, a charge of 0.174 mC cm^{-2} is required to form a monolayer of $Fe(OH)_2$(0001) film. On the other hand, the charge consumption of peak (A_1) estimated from the CV shown in Fig. 5-1

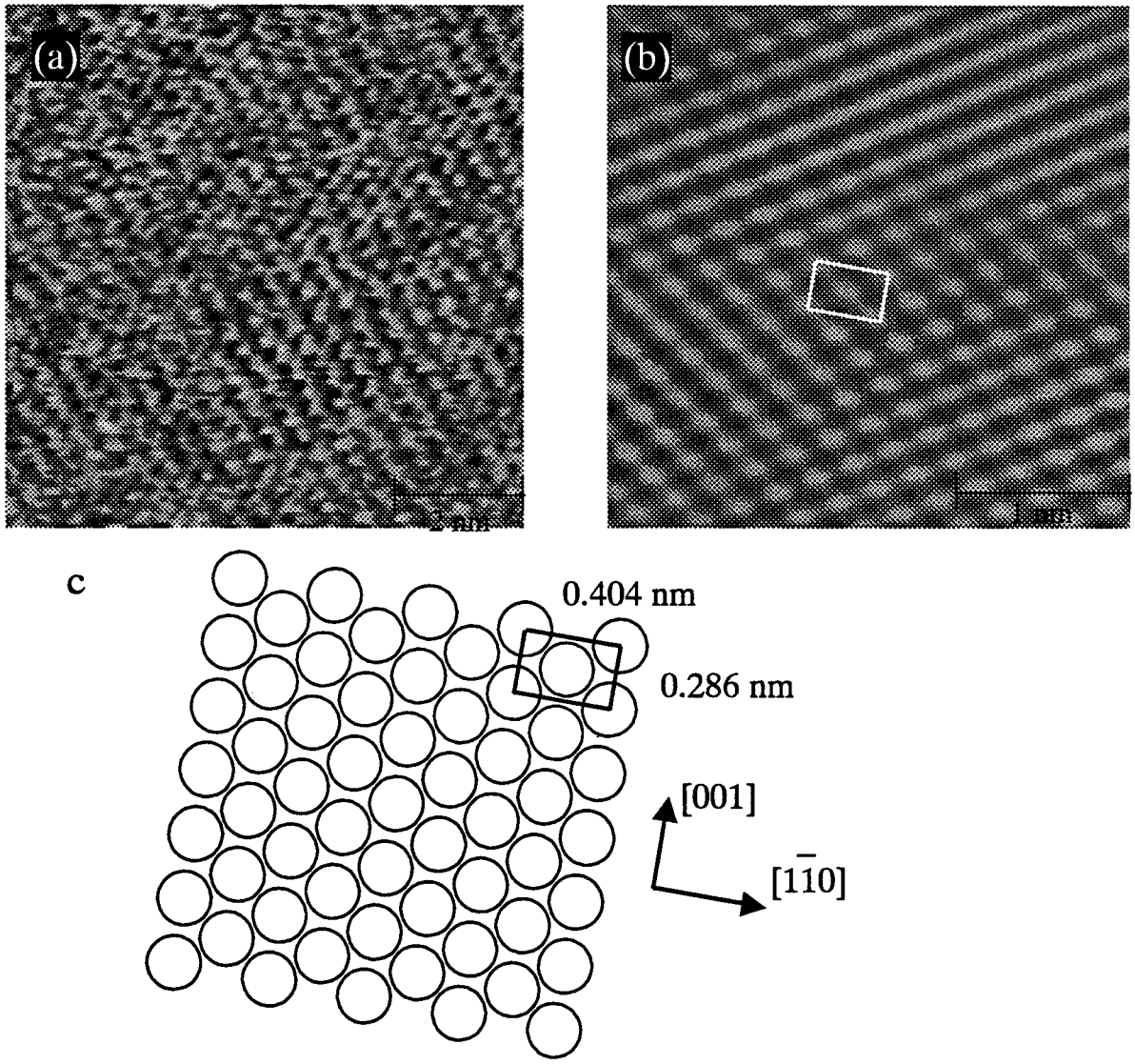

Figure 5-2 (a) *In-situ* atomic resolution EC-AFM image of Fe(110) obtained at –1.25 V in 0.05 M Na_2SO_4 aqueous solution after keeping the potential in hydrogen evolution region and removing the oxide layer off the iron surface by means of the AFM cantilever. (b) Filtered image of image (a). (c) Schematic model of the Fe(110)-(1×1) plane.

was 0.2 ± 0.05 mC cm $^{-2}$. If the effect of peak (A_2) was ignored at –0.55V, the thickness of $Fe(OH)_2$(0001) film formed on Fe(110) electrode is estimated to be only one monolayer at –0.55 V.

After combining the Figs. 5-2 and Figs. 5-3, it is found that the atomic rows along the

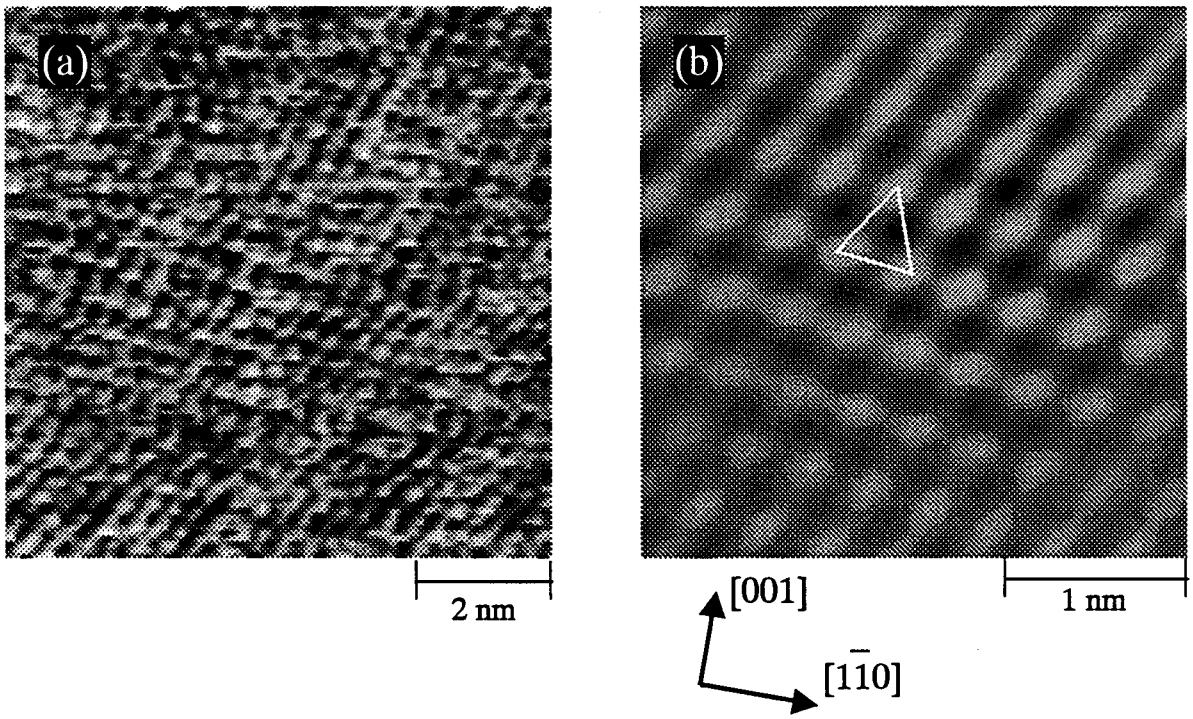

Figure 5-3 (a) *In-situ* atomic resolution EC-AFM image of Fe(110) obtained at –0.55 V in 0.05 M Na_2SO_4 aqueous solution. (b) Filtered image of image (a).

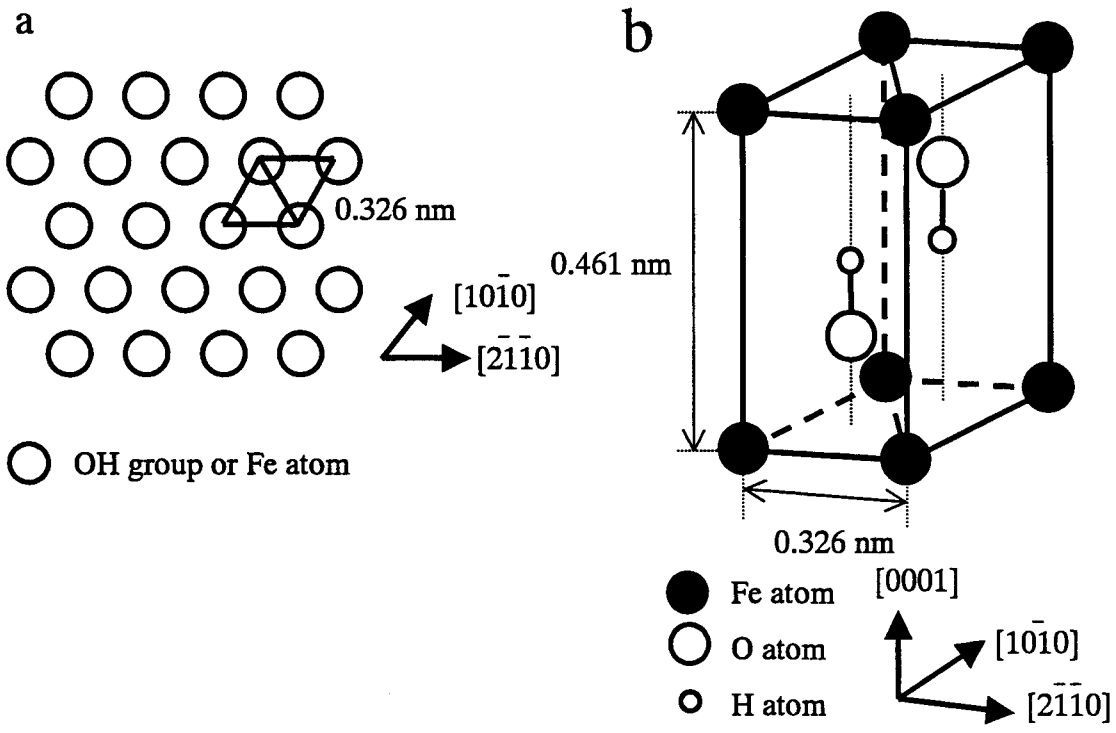

Figure 5-4 Schematic model of the $Fe(OH)_2(0001)$-(1×1) plane (a) and of the bulk $Fe(OH)_2$ structure (b).

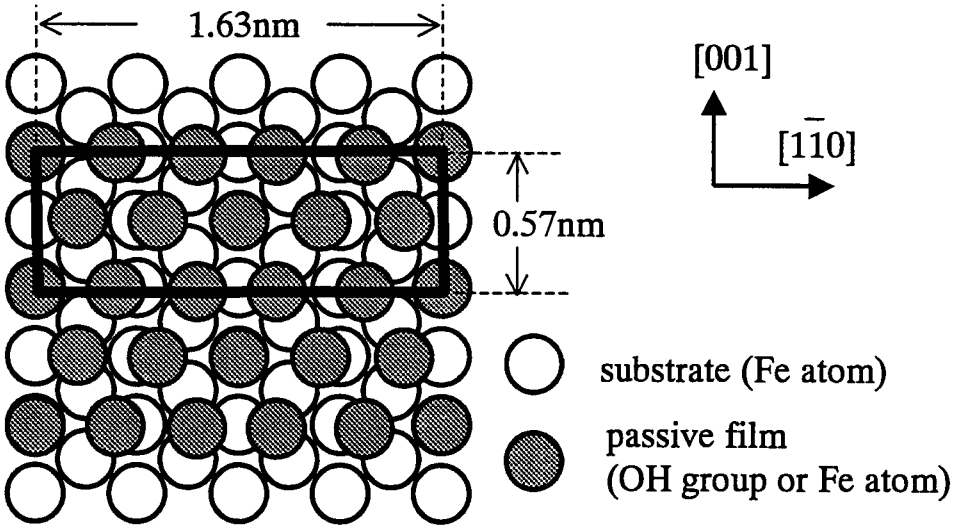

Figure 5-5 Schematic model of the $Fe(OH)_2(0001)$-(1×1) plane on Fe(110)-(1×1) substrate.

[2$\bar{1}$0] direction of $Fe(OH)_2(0001)$ surface was parallel with those along the [1$\bar{1}$0] direction of Fe(110) surface as shown in Fig. 5-5. This $Fe(OH)_2(0001)$ // Fe(110) epitaxial system has small lattice constant misfit of 1.3 % along [001] direction. Along [1$\bar{1}$0] direction, there is large misfit of 19.3 %, but the misfit between 5 times of the $Fe(OH)_2$ periodicity and 4 times that of the Fe(110) is less than 1 %. Such a long-scale epitaxial relationship between the anodic oxide layers and the metal substrates was also observed in the case of the $Cu_2O(111)$ // Cu(111) [33], NiO(111) (or $Ni(OH)_2(0001)$) // Ni(111) [35,36] and $Co(OH)_2(0001)$ // Co(0001) [37].

IV. Conclusion

Fe(110) single crystal electrodes in 0.05 M Na_2SO_4 aqueous solution under the control of potential were investigated by *in-situ* EC-AFM. Keeping the potential at –1.85 V and repeated scanning the surface with the AFM cantilever for 10 minutes yielded to remove the oxide layer off the iron surface and I observed an unreconstructed Fe(110)-(1×1) structure at –1.25 V in 0.05 M Na_2SO_4 aqueous solution. This is the first atomic image of bare Fe(110)-(1×1) obtained in solution. $Fe(OH)_2(0001)$-(1×1) structure of the anodic oxide layer on Fe(110) single crystal was observed at –0.55 V in 0.05 M Na_2SO_4 aqueous solution by *in-situ* EC-AFM. It was found that the anodic oxide layer and Fe(110) substrate had an epitaxial relationship of $Fe(OH)_2$ (0001) [2$\bar{1}\bar{1}$0]

// Fe(110) [$1\bar{1}0$] and that the misfit between the anodic oxide layer and Fe(110) substrate was less than 1.3%.

References

[1] M. E. Brett, K. M. Parkin and M. J. Graham, J. Electrochem. Soc., **133** (1986) 2031.

[2] S. Haupt and H. Strehblow, Langmuir, **3** (1987) 873.

[3] E. McCafferty, M. K. Bernett and J. S. Murday, Corros. Sci., **28** (1988) 559.

[4] E. B. Castro, J. R. Vilche and A. J. Arvia, Corros. Sci., **32** (1991) 37.

[5] J. Benzakour and A. Derja, J. Electroanal. Chem., **437** (1997) 119.

[6] M. Seo, J. B. Lumsden and R. W. Staehle, Surf. Sci., **50** (1975) 541.

[7] R. W. Revie, B. G. Baker and J. O'M. Bocklis, J. Electrochem. Soc., **122** (1975) 1460.

[8] R. Goetz, B. MacDougall and M. J. Graham, Electrochim. Acta, **31** (1986) 1299.

[9] J. R. Gancedo, C. Alonso, C. Andrade and M. Gracia, Corrosion, **122** (1989) 976.

[10] W. E. O'Grady, J. Electrochem. Soc., **127** (1980) 555.

[11] Y. Y. Esipenko and A. M. Sukhotin, Prot. Met., **24** (1989) 285.

[12] E. Kuzmann, M. L. Varsanyi, A. Vertes and W. Meisel, Electrochim. Acta, **36** (1991) 911.

[13] C. S. Vertes, M. L. Varsanyi, A. Vertes, W. Meisel and P. Guetlich, Electrochim. Acta, **38** (1993) 2253.

[14] R. Goetz, D. F. Mitchell, B. MacDougall and M. J. Graham, J. Electrochem. Soc., **134** (1987) 535.

[15] J. A. Bardwell, B. MacDougall and M. J. Graham, J. Electrochem. Soc., **135** (1988) 413.

[16] E. V. Lisovaya, A. M. Sukhotin, P. P. Konorov and Y. A. Tarantov, Sov. Electrochem., **22** (1986) 792.

[17] E. V. Lisovaya, A. M. Sukhotin, P. P. Konorov and Y. A. Tarantov, Sov. Electrochem., **22** (1986) 845.

[18] A. G. Borzenko and V. A. Safonov, Prot. Met., **24** (1989) 429.

[19] H. W. Shen, S. Z. Szklarska, Corrosion, **45** (1989) 720.

[20] R. Nishimura and N. Sato, ISIJ International, **31** (1991) 177.

[21] V. A. Safonov and E. V. Lapshina, Prot. Met., **26** (1991) 413.

[22] C. A. Melendres, J. Acho and R. L. Knight, J. Electrochem. Soc., **138** (1991) 877.

[23] J. Gui and T. M. Devine, Corros. Sci., **32** (1991) 1105.

[24] D. Sazou, M. Pagitsas and C. Georgolios, Electrochi. Acta, **37** (1992) 2067.

[25] L. J. Oblonsky and T. M. Devine, Corros. Sci., **37** (1995) 17.

[26] J. Gui and T. M. Devine, Corros. Sci., **37** (1995) 1177.

[27] T. Ohtsuka, Mater. Trans. JIM, **37** (1996) 67.

[28] M. Buchler, P. Schmuki and H. Bohni, J. Electrochem. Soc., **144** (1997) 2307.

[29] M. Buchler, P. Schmuki and H. Bohni, J. Electrochem. Soc., **145** (1998) 609.

[30] L. J. Oblonsky A. J. Davenport, M. P. Ryan, H. S. Isaacs and R. C. Newman, J. Electrochem. Soc., **144** (1997) 2398.

[31] K. Fushimi, K. Azumi and M. Seo, ISIJ international, **39** (1999) 346.

[32] B. J. Cruickshank, D. D. Sneddon and A. A. Gewirth, Surf. Sci., **281** (1993) L308.

[33] N. Ikemiya, T. Kubo and S. Hara, Surf. Sci., **323** (1995) 81.

[34] S.- L. Yau, F.- R. F. Fan, T. P. Moffat and A. J. Bard, J. Phys. Chem., **98** (1994) 5493.

[35] T. Suzuki, T. Yamada and K. Itaya, J. Phys. Chem., **100** (1996) 8954.

[36] N. Hirai, H. Okada and S. Hara, in preparation.

[37] S. Ando, T. Suzuki and K. Itaya, J. Electroanal. Chem., **431** (1997) 277.

[38] R. C. Bhardwaj, A. G.- Martín and J. O'M Bockris, J. Electrochem. Soc., **138** (1991) 1901.

[39] J. Li and D. J. Meier, J. Electroanal. Chem., **454** (1998) 53.

[40] C. Liu and P. M. Huang, Soil Sci. Soc. Ame. J., **63** (1999) 65.

[41] B. M.- Zülow, S. Kipp, R. Lacmann and M. A. Schneeweiss, Surf. Sci., **311** (1994) 153.

[42] O. Khaselev and J. M. Sykes, Electrochim. Acta, **42** (1997) 2333.

[43] M. P. Ryan, R. C. Newman and G. E. Thompson, J. Electrochem. Soc., **142** (1995) L177.

[44] K. Takahashi, J. A. Bardwell, B. MacDougall and M. J. Graham, Electrochim. Acta, **37** (1992) 477.

[45] M. Pourbaix, Atlas of Electrochemical Equilibria in Aqueous Solution, 1st English ed., Pergamon Press, Oxford (1966) 307.

Chapter 6.

Electrodeposition of II – IV Semiconductor Thin Films on Gold Single Crystal

I. Introduction

As shown in the preceding chapters, it is known that clean and bare surfaces of metals, such as gold, silver, copper, iron, and so on, can be observed by EC-AFM, even in aqueous solution. Many researchers have tried to electrodeposit epitaxial films on such clean and bare surfaces, especially on gold. *In-situ* AFM [1-4] and STM [5] have been used to investigate the growth of epitaxial films in aqueous solution. For example, Ikemiya *et al.* found that the extremely flat Ag(100)-(1×1) films were formed by a Frank-van der Merwe (FM) mode even at a high deposition rate (~7.2 monolayers(ML) per minutes) on Au(100) substrate in sulfuric acid solution, while the Te films, consisted of three epitaxial layers of the first ($\sqrt{2}\times\sqrt{2}R45^\circ$) (~10 ML), the second $c(\sqrt{2}\times 3\sqrt{2})R45^\circ$ (20~30 ML) and the third Te($10\bar{1}0$)(80 ML~) structure atop, were formed by a Stranski-Krastanov (SK) mode even at a low deposition rate (~0.5 ML /min.) on the same substrate in the sane solution [3,4].

In the meantime, the studies on co-electrodeposition of IIb and VIb elements are interesting because it is expected to provide a low-cost room-temperature and large-scale production route of II-VI compound semiconductor films, which are candidates of photoelectric and quantum devices with high efficiency. Electrodeposition of II-VI compound semiconductor films is roughly divided into three methods shown below.

The most traditional method is an overpotential deposition (OPD) of both IIb and VIb elements, which electrodeposit under the control of their own concentration [6]. Although an extremely high deposition rate and a suitable composition ratio of IIb and VIb elements may be achieved by this method, the simultaneous control on the concentration of both elements may be very difficult in practice and hence the electrodeposited films may contain some parts being far

from the desired composition.

The second one is an alternative underpotential deposition (UPD) of IIb and VIb elements, namely, electrochemical atomic layer epitaxy (EC-ALE) [7], which is the electrochemical analogue of atomic layer epitaxy (ALE) [8]. Stickney and his co-worker have enthusiastically investigated to form many kinds of compound semiconductor films, such as CdTe [7,9-16], CdSe [15,17], CdS [15,18], ZnTe [19], ZnSe [19], ZnS [19], GaAs [20,21], and so on, by this EC-ALE methodology. The epitaxial relationship between the electrodeposited films with one or two layers thickness and the low-index Au substrates have been revealed by low energy electron diffraction (LEED) [10,12,20,21] and STM [13,22]. However, the proposed system for formation of films is very complicated [14], and moreover, surface roughening on a sub-micron scale is observed for the films with more than 0.3 μm on thickness [15].

The third method is first proposed by Panicker *et al.* [23]. It's an OPD of the VIb element, only onto which the IIb element can deposit from the strong mutual interaction between the VIb and IIb elements. In other words, deposition of the IIb element is carried out as an UPD on a VI element surface deposited overpotentially. However, all previous works have resulted in polycrystalline films formed by a SK mode up to now except the nanocrystalline of CdSe on gold [24]. I think that extremely low concentration of the VIb element in the electrolyte nearby the electrode is indispensable in order to form films with high quality. This chapter shows the electrodeposition processes of CdTe and CdSe thin films on gold, which are the preliminary studies of formation of epitaxial II-VI semiconductor films in solution. Those processes have been investigated by electrochemical methods and X-ray photoelectron Spectroscopy (XPS),

II. Experimental

Au(111) single crystals or Au(111) vapor-deposited on polyethylene (supplied from Tanaka Kikinzoku Kogyo, Au(111)/PE) films were used as substrates. The advantages of Au(111) as substrates are that gold is stable at potential to deposit in comparison with the other metals [9], and that an final UPD structure of Te on Au(111) in sulfuric acid solution is (3×3)-Te [2], which corresponds to CdTe($\bar{1}\bar{1}\bar{1}$) with misfit of 5 %, as shown in Fig. 6-1.

The characteristics of Au(111)/PE films to be cut and bent easily are beneficial to their application for the solar cell. In order to confirm the (111) orientation of Au(111)/PE films, X-ray diffraction (XRD) patterns of Au(111)/PE and also that of polyethylene film were measured by

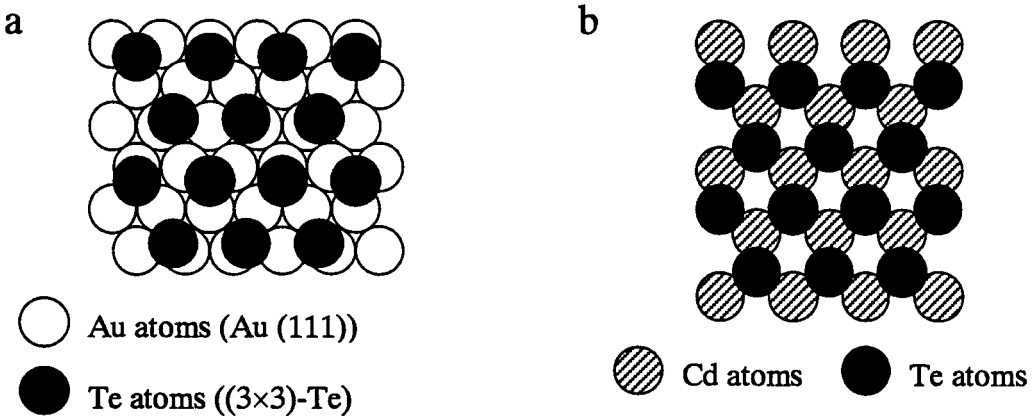

Figure 6-1 Structural models of (a) a final UPD structure of Te on Au(111) substrate and (b) CdTe ($\bar{1}\bar{1}\bar{1}$) structure.

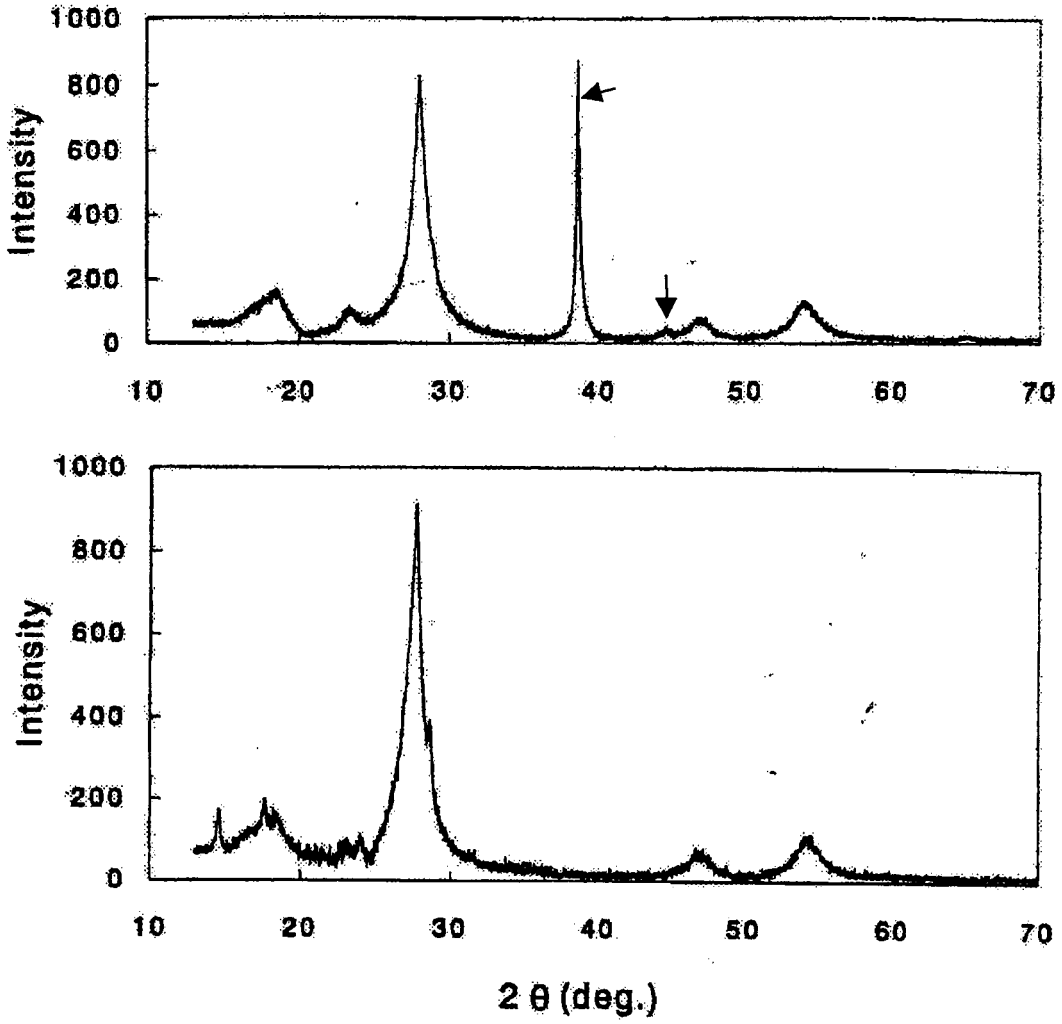

Figure 6-2 X-ray diffraction patterns of (a) Au(111)/polyethylene and (b) polyethylene.

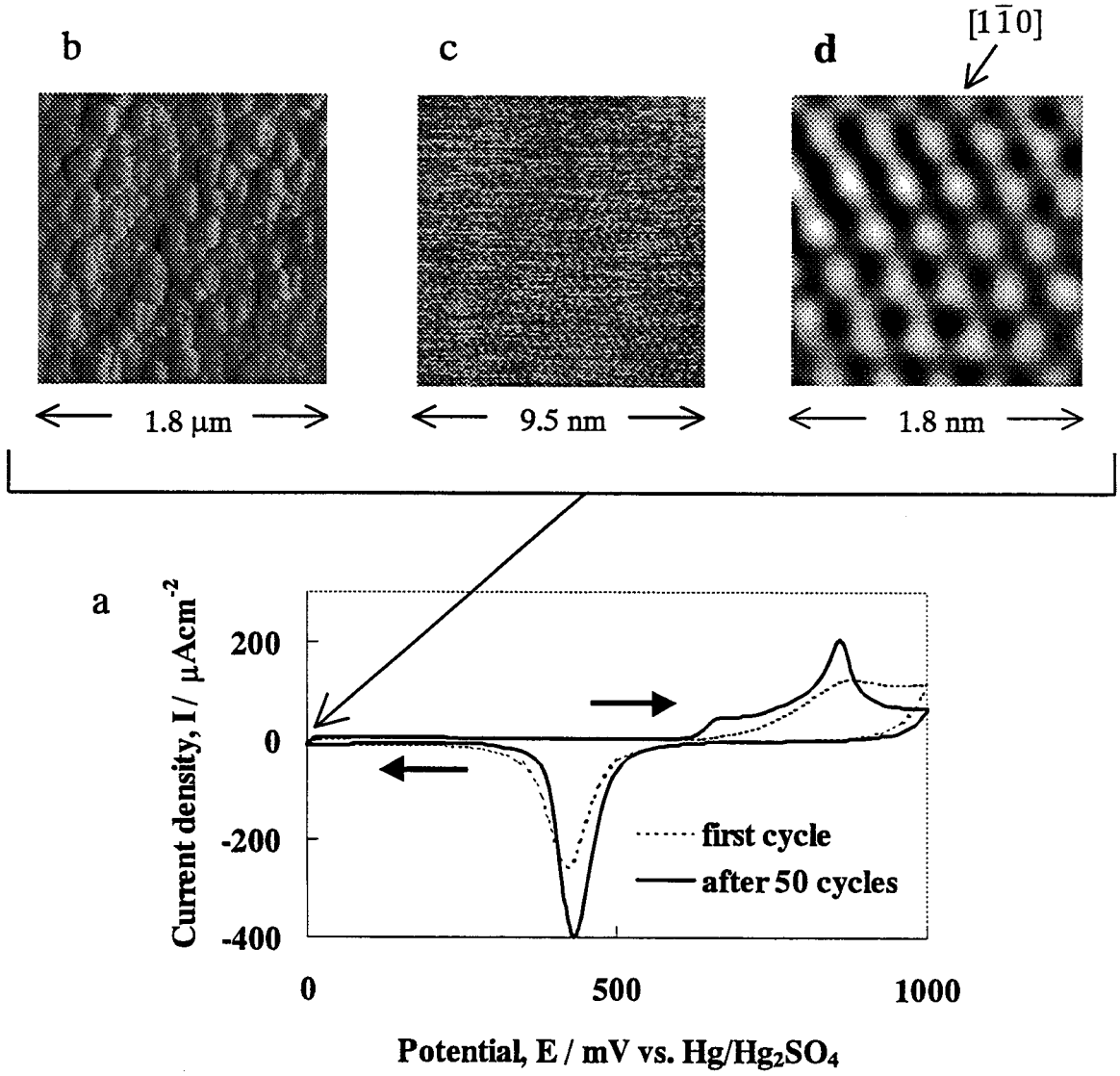

Figure 6-3 (a) Cyclic voltammograms for Au(111)/ polyethylene in 0.05 M H_2SO_4 solution with sweep rate of 50 mV sec $^{-1}$, together with AFM images (b-d). (b) Large scale (1.8 ×1.8 μm) and (c) unfiltered atomic resolution (9.5×9.5 nm) images obtained at 0 V after 50 potential cycles between 0 and 1 V. (d) Filtered and enlarged image (1.8×1.8 nm) of (c), showing an unreconstructed Au(111) structure. The [1$\bar{1}$0] direction indicated by an arrow.

XD-5A(Shimazu), and the results are as shown in Fig.6-2.

Figure 6-3 shows CVs for Au(111)/ polyethylene in 0.05 M H_2SO_4 solution with sweep rate of 50 mV sec^{-1}, together with AFM images (b-d). After 50 potential cycles between 0 and 1 V, the shape of CV for Au(111)/ PE became similar to that for Au(111) single crystals [25] and after that an *in-situ* EC-AFM image in Fig. 6-3(b) was taken at 0 V. This image indicates that a Au(111)/PE film consists of aggregated grains of approximately 100~200 nm. On any grains, an *in-situ* EC-AFM image with atomic resolution was obtained at 0 V, as shown in Fig. 6-3(c). From the filtered image of (c), shown in Fig. 6-3(d), we can recognize the protrusions (white spots) having three-fold symmetry with interatomic distance of 0.29 nm. That corresponds well to an unreconstructed Au(111)-(1×1) structure. Considering the results mentioned above, these are not inferior to Au(111) single crystal at all. Actually, the results for Au(111)/PE is not so different from that for Au(111) single crystal in these experiments, so that no mention on the substrate is denoted in the following paragraph.

The reference electrode used here was the Hg/Hg_2SO_4 electrode, to which all potential was referred in this chapter. The electrolytes used were prepared from H_2SO_4 (Wako, Superior), $CdSO_4$ (Wako), TeO_2(Rare Metallic), SeO_2(Rare Metallic) and MilliQ-water, and they were deaerated with Ar gas for more than 1 hour before each experiment.

The XPS spectra were taken by XPS-7000(RIGAKU) at a pressure of $1\sim2\times10^{-7}$ Pa. A magnesium X-ray source (1253.6 eV) was used for all works. The calibration in all cases was referred to the Au $4f_{7/2}$ electron peak at 83.8 eV due to gold substrates. Before the XPS analysis, the films were transferred in air from the electrochemical cell and then to the chamber for XPS.

III. Results and discussion

III-1. Cyclic voltammetry (VIb element = Te)

All of CVs for Au(111) shown in Figs. 6-4 are taken at the sweep rate of 10 mV sec^{-1}. Figures 6-4(a), (b) and (c) are for those in 0.05 M H_2SO_4 + 10^{-3} M $CdSO_4$, in 0.05 M H_2SO_4 + 10^{-4} M TeO_2, and in 0.05 M H_2SO_4 + 10^{-3} M $CdSO_4$ + 10^{-4} M TeO_2 aqueous solution, respectively.

The CV in Fig. 6-4(a), denoted by C for anodic processes and by A for cathodic ones, indicates that peaks due to the Cd -UPD (C_1, A_1), those due to the Cd- OPD (C_2, A_2) and those due to surface alloying at the Cd/Au interface (C_3, A_3) were detected. This CV is fairly in good agreement with that reported in the previous work [26].

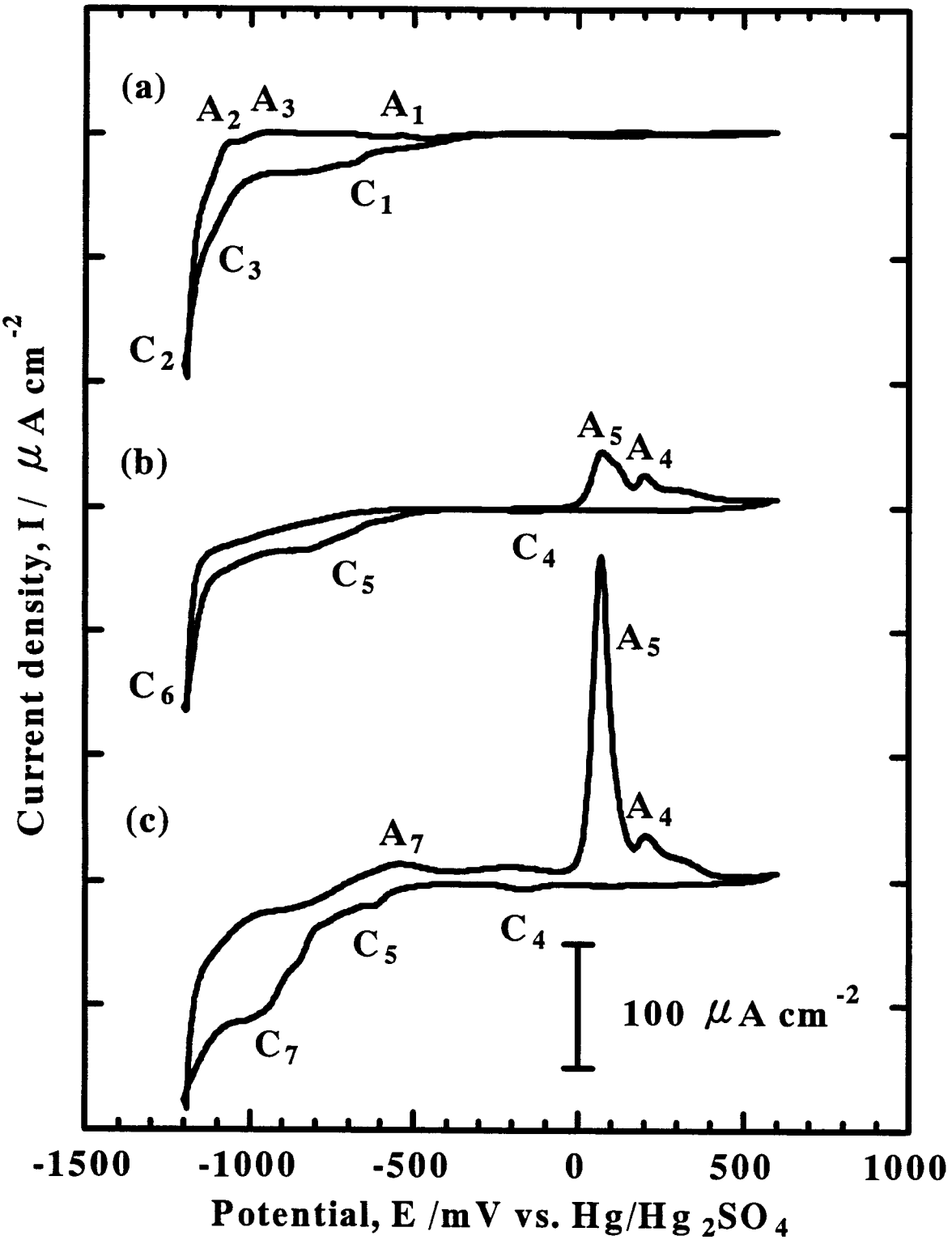

Figure 6-4 Cyclic voltammograms for Au(111) in (a) 0.05 M H_2SO_4 + 10^{-3} M $CdSO_4$ (b) 0.05 M H_2SO_4 + 10^{-4} M TeO_2 and (c) 0.05 M H_2SO_4 + 10^{-3} M $CdSO_4$ + 10^{-4} M TeO_2 aqueous solution with sweep rate of 10 mV sec^{-1}.

From the CV in Fig. 6-4(b) for 0.05 M H_2SO_4 + 10^{-4} M TeO_2 aqueous solution, peaks due to the Te- UPD (C_4, A_4) and the Te- OPD (C_5, A_5) were observed. This CV also practically agrees with that reported in the previous work [4]. In addition to these peaks described above, a cathodic peak is observed at –1.2 V, which is considered to correspond dissolution of electrodeposited Te that is given by the following equation [27],

$$Te(s) + 2H^{2+} + 2e^- \Rightarrow H_2Te\ (g). \qquad (6\text{-}1)$$

The interpretation on this cathodic peak is consistent with the fact that the anodic peak of Te OPD (A_5) in the CV between –1.2 V and 0.6 V is smaller than that in the CV between –1.0 V to 0.6 V.

In the case of the CV in Fig. 6-4(c), two new peaks, that is, a cathodic one at –0.9 V and an anodic one at –0.6 V appeared in addition to the peaks observed in Figs. 6-4(a) and (b). It is considered that those peaks are correspond to the formation and dissolution of CdTe given by the following electrochemical reaction,

$$Te(s) + Cd^{2+} + 2e^- \Leftrightarrow CdTe\ (s), \qquad E_0 \approx -0.70V. \qquad (6\text{-}2)$$

It is also noteworthy that the A_5 peak in the CV between –1.2 and 0.6 V is extremely bigger that in the CV between –1.0 and 0.6 V in this solution. It strongly suggests that the Te dissolution by the Eq. (6-1) was suppressed due to the CdTe formation given by Eq. (6-2).

III-2. Cyclic voltammetry (VIb element = Se)

In the case of Se as VIb element, similar results were obtained. Figure 6-5 show CVs for Au(111) taken at the sweep rate of 10 mV sec^{-1}. Figures 6-5(a), (b) and (c) are those in 0.05 M H_2SO_4 + 10^{-3} M $CdSO_4$, in 0.05 M H_2SO_4 + 10^{-4} M SeO_2 and in 0.05 M H_2SO_4 + 10^{-3} M $CdSO_4$ + 10^{-4} M SeO_2 aqueous solution, respectively.

The following results are obtained.

(1) It is considered that the cathodic peak (C_7) at –0.6 V and the anodic peak (A_7) at –0.4 in Fig. 6-5(c) are correspond to the formation of CdSe given by the following electrochemical reaction,

$$Se(s) + Cd^{2+} + 2e^- \Leftrightarrow CdSe\ (s), \qquad E_0 \approx -0.47\ V. \qquad (6\text{-}3)$$

(2) The cathodic peak (C_6) at –0.7 V observed in Fig. 6-5(b) is considered to be caused by the Se dissolution, that is, the following electrochemical reaction [28],

$$Se(s) + 2H^{2+} + 2e^- \Rightarrow H_2Se\ (g), \qquad (6\text{-}4)$$

and this reaction could be suppressed under the presence of Cd^{2+} ions, as shown in Fig. 6-5(c).

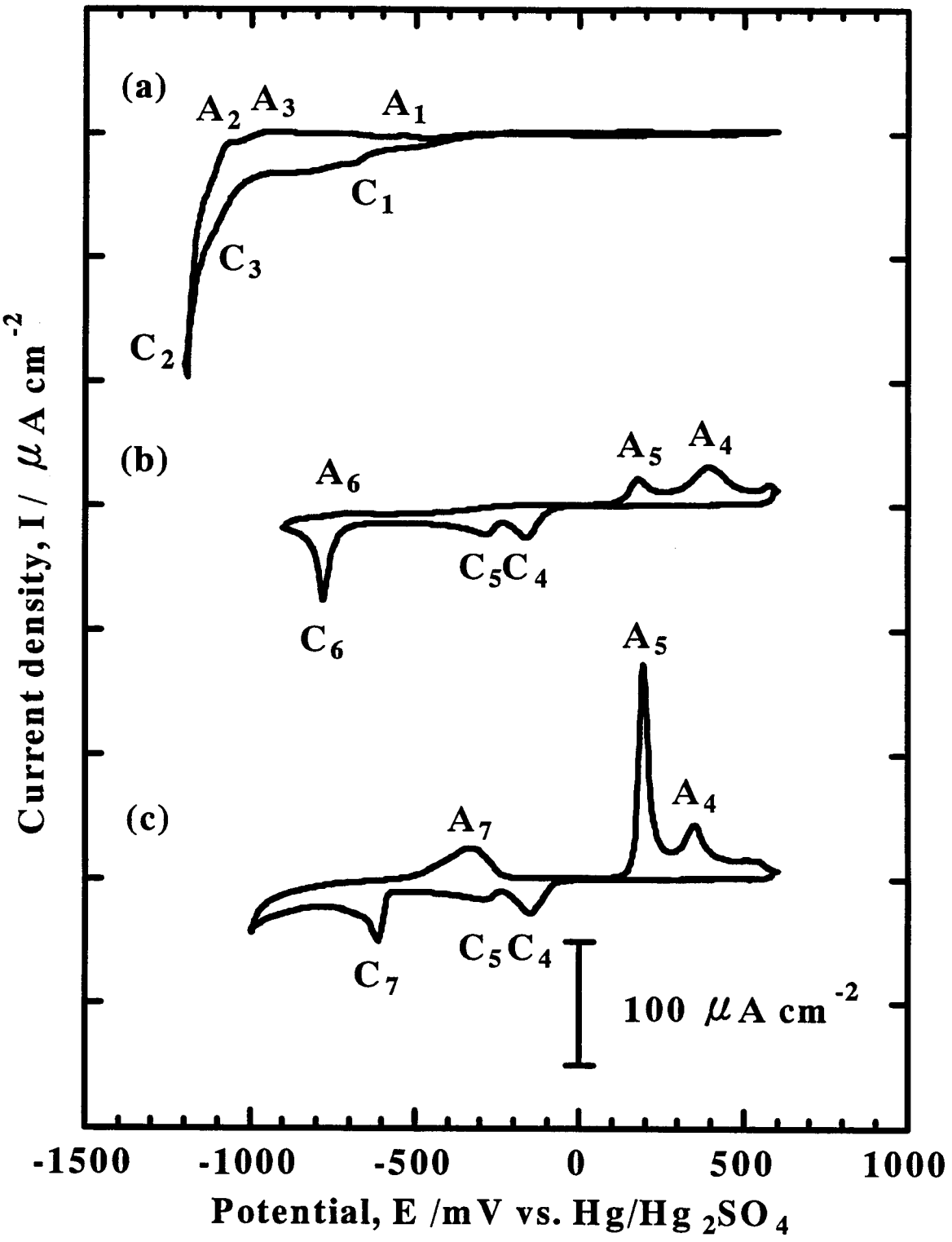

Figure 6-5 Cyclic voltammograms for Au(111) in (a) 0.05 M H_2SO_4 + 10^{-3} M $CdSO_4$ (b) 0.05 M H_2SO_4 + 10^{-4} M SeO_2 and (c) 0.05 M H_2SO_4 + 10^{-3} M $CdSO_4$ + 10^{-4} M SeO_2 aqueous solution with sweep rate of 10 mV sec^{-1}.

III-3. X-ray photoelectron spectroscopy (VIb element = Te)

The XPS spectra were measured only in the case that VIb element is Te. The film electrodeposited at –1.0 V for 30 minutes in 0.05 M H_2SO_4 + 10^{-3} M $CdSO_4$ + 10^{-4} M TeO_2 aqueous solution, which is called "sample(Cd+Te)", was investigated by XPS. At this deposition potential, the OPD of Cd does not occur. The thickness of sample(Cd+Te) estimated from the deposition current is about 20 nm. In order to compare with sample(Cd+Te), the film electrodeposited at –1.2 V for 30 minutes in 0.05 M H_2SO_4 + 10^{-3} M $CdSO_4$ aqueous solution (sample(Cd)) and the film electrodeposited at –0.8 V for 30 minutes in 0.05 M H_2SO_4 + 10^{-4} M TeO_2 aqueous solution (sample(Te)) were also investigated. XPS spectra of each sample were recorded both before and after Ar sputtering for 5 sec.

Table 6-1 XPS analysis of Cd 3d peaks for electrodeposited samples

Sample	Element(orbit)	Peak Energy(eV)	FWHM(eV)	Chemical Shift(eV)
Sample(Cd) *)	$Cd(3d)_{3/2}$	412.1	1.83	0.3
(as prepared)	$Cd(3d)_{5/2}$	405.3	1.91	0.2
Sample(Cd) *)	$Cd(3d)_{3/2}$	411.8	1.21	0
(after sputtering)	$Cd(3d)_{5/2}$	405.1	1.31	0
Sample(Cd+Te) **)	$Cd(3d)_{3/2}$	412.2	1.24	0.4
(as prepared)	$Cd(3d)_{5/2}$	405.4	1.30	0.3
Sample(Cd+Te) **)	$Cd(3d)_{3/2}$	412.1	1.23	0.3
(after sputtering)	$Cd(3d)_{5/2}$	405.3	1.27	0.2

*) Sample(Cd) is the film deposited at –1.2 V for 30 min. in 0.05 M H_2SO_4 + 10^{-3} M $CdSO_4$ aqueous solution.

**) Sample(Cd+Te) is the film deposited at -1.2 V for 30 min. in 0.05 M H_2SO_4 + 10^{-3} M $CdSO_4$ + 10^{-4} M TeO_2 aqueous solution.

Table 6-1 shows energies of Cd 3d electron peaks of sample(Cd) and sample(Cd+Te) and their FWHM. The shifts from the Cd 3d peaks of sample(Cd) after Ar sputtering are referred to "chemical shifts". It should be noted that Cd 3d electron peaks were also detected for the sample(Cd+Te) as prepared, though the OPD of Cd does not occur at the potential. Table 6-2

Table 6-2 XPS analysis of Te 3d peaks for electrodeposited samples

Sample	Element(orbit)	Peak Energy(eV)	FWHM(eV)	Chemical Shift(eV)
Sample(Te) *) (as prepared)	$Te(3d)_{3/2}$	587.4	1.65	3.6
		583.8	1.58	0
	$Te(3d)_{5/2}$	577.0	1.81	3.5
		573.5	1.67	0
Sample(Te) *) (after sputtering)	$Te(3d)_{3/2}$	583.8	1.73	0
	$Te(3d)_{5/2}$	573.5	1.87	0
Sample(Cd+Te) **) (as prepared)	$Te(3d)_{3/2}$	583.4	1.49	-0.4
	$Te(3d)_{5/2}$	573.0	1.56	-0.5
Sample(Cd+Te) **) (after sputtering)	$Te(3d)_{3/2}$	583.2	1.55	-0.6
	$Te(3d)_{5/2}$	572.9	1.54	-0.6

*) Sample(Te) is the film deposited at –0.8 V for 30 min. in 0.05 M H_2SO_4 + 10^{-4} M TeO_2 aqueous solution.

**) Sample(Cd+Te) is the film deposited at -1.2 V for 30 min. in 0.05 M H_2SO_4 + 10^{-3} M $CdSO_4$ + 10^{-4} M TeO_2 aqueous solution.

shows energies of Te 3d electron peaks of sample(Te) and sample(Cd+Te) and their FWHM and Fig. 6-6 shows examples of the spectra. As shown in Fig. 6-6(a), four peaks were observed, whereas two peaks in Fig. 6-6(b). It is considered that surface oxide layer of the film was removed by Ar sputtering, so that the two peaks removed after Ar sputtering are due to the existence of tellurium dioxide (Te^{4+}). It is noteworthy that the peaks for the sample(Cd+Te) as prepared due to tellurium dioxide are much smaller than that for sample(Cd) as prepared. It should be also emphasized that chemical shifts for sample(Cd+Te) both before and after Ar sputtering are –0.4~0.6 eV, which is similar to the reported mean value for Te^{-2} of –0.7 eV [29]. These results indicates that the sample(Cd+Te) are mainly composed of CdTe and is not easily oxidized.

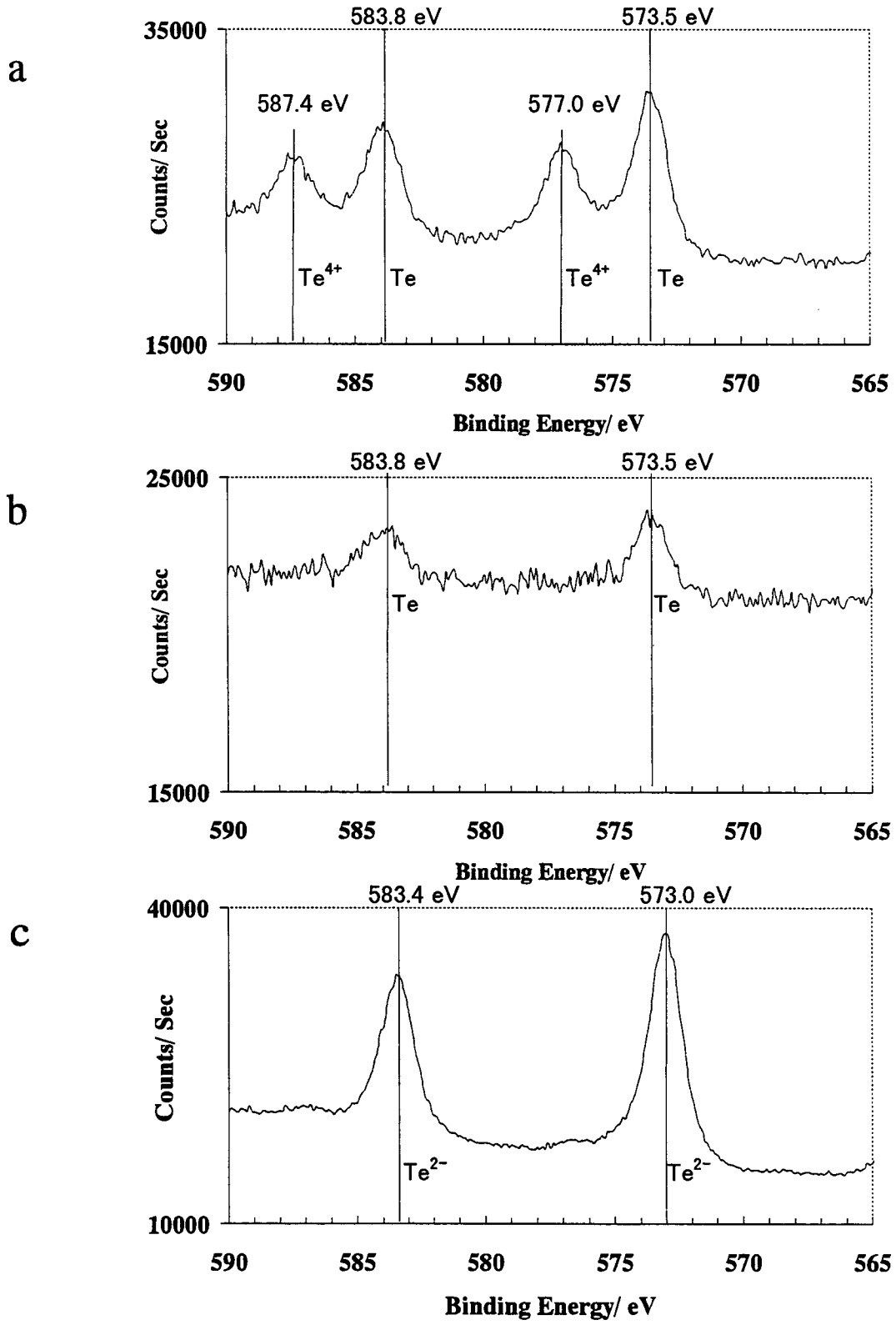

Figure 6-6 XPS spectra of Te 3d regions of (a) Sample(Te) as prepared, (b) Sample(Te) after Ar sputtering and (c) Sample(Cd+Te) as prepared.

IV. Conclusion

The electrodeposition in sulfuric acid solution containing both IIb and VIb elements was investigated by electrochemical methods and X-ray photoelectron Spectroscopy (XPS). The CV in the solution containing both IIb and VIb elements has one cathodic and one anodic peaks which can not observe in the solution containing either IIb or VIb elements, and it is found that these peaks are due to the formation and dissolution of II-VI compound semiconductor. From XPS analysis for the film electrodeposited in the solution containing both Cd and Te at the potential of –1.0 V, where the OPD of Cd does not occur, it is found that this electrodeposited film is mainly composed of CdTe and it's not easily oxidized.

References

[1] N. Ikemiya, S. Miyaoka and S. Hara, Surf. Sci., **327** (1995) 261.

[2] N. Ikemiya, K. Yamada and S. Hara, Surf. Sci., **348** (1996) 253.

[3] N. Ikemiya, K. Yamada and S. Hara, J. Vac. Sci. & Technol. B, **14** (1996) 1369.

[4] N. Ikemiya, D. Iwai, K. Yamada, R. Vidu, S. Hara, Surf. Sci. **369** (1996) 199.

[5] H. Naohara, S. Ye and K. Uosaki, J. Phys. Chem. B, **102** (1998) 4366.

[6] H. Gobrecht, H. D. Liess and a. Tausend, Ber. Dtsch. Bunsenges. Phys. Chem., **67** (1973) 930.

[7] B. W. Gregory and J. L. Stickney, J. Electroanal. Chem., **300** (1991) 543.

[8] M. Pessa, R. Makela and R. Suntola, Appl. Phys. Lett., **38** (1980) 131.

[9] B. W. Gregory, M. L. Norton and J. L. Stickney, J. Electroanal. Chem., **293** (1990) 85.

[10] B. W. Gregory, D. W. Suggs and J. L. Stickney, J. Electrochem. Soc., **135** (1991) 1279.

[11] D. W. Suggs, I. Villegas, B. W. Gregory and J. L. Stickney, J. Vac. Sci. Technol. A, **10** (1992) 886.

[12] D. W. Suggs and J. L. Stickney, Surf. Sci., **290** (1993) 362.

[13] D. W. Suggs and J. L. Stickney, Surf. Sci., **290** (1993) 375.

[14] B. M. Huang, L. P. Colletti, B. W. Gregory, J. L. Anderson and J. L. Stickney, J. Electrochem. Soc., **142** (1995) 3007.

[15] L. P. Colletti, B. H. Flowers Jr. and J. L. Stickney, J. Electrochem. Soc., **145** (1998) 1442.

[16] L. P. Colletti and J. L. Stickney, J. Electrochem. Soc., **145** (1998) 3594.

[17] T. E. Lister and J. L. Stickney, Appl. Surf. Sci., **107** (1996) 153.

[18] L. P. Colletti, D. Telkay and J. L. Stickney, J. Electroanal. Chem., **396** (1994) 145.

[19] L. P. Colletti, S. Thomas, E. M. Wilmer and J. L. Stickney, Mat. Res. Soc. Symp. Proc., **451** (1997) 235.

[20] I. Villegas and J. L. Stickney, J. Electrochem. Soc., **139** (1992) 686.

[21] I. Villegas and J. L. Stickney, J. Vac. Sci. Technol. A, **10** (1992) 3032.

[22] B. E. Hayden and I. S. Nandhakumar, J. Phys. Chem. B, **102** (1998) 4897.

[23] M. P. R. Panicker, M. Knaster and F. A. Kroger: J. Electrochem. Soc. 125 (4), 566 (1978).

[24] Y. Golan, S. Cohen, I. Rubinstein and G. Hodes, Langmuir, **8** (1992) 749.

[25] N. Ikemiya, S. Miyaoka and S. Hara, Surf. Sci., **311** (1994) L641.

[26] R. Vidu and S. Hara, Inter. Symp. Designing, Processing and Properties of Adv. Eng. Mat., (1997) 541.

[27] M. Pourbaix, Atlas of Electrochemical Equilibria in Aqueous Solution, 1st English ed., Pergamon Press, Oxford (1966) 560.

[28] M. Pourbaix, Atlas of Electrochemical Equilibria in Aqueous Solution, 1st English ed., Pergamon Press, Oxford (1966) 554.

[29] Y. Nihei, Bunseki (1987) 836.

Chapter 7.

Summary

Metal/ electrolyte interface is important from not only fundamental aspects, but also practical applications, for example, batteries, however, there is lack of information about influence of the high electric field at metal/electrolyte interface on the atoms located on metal surface. Therefore, I have investigated the behavior of electrified metal surface in contact with aqueous solution using the *in-situ* EC-AFM, which can directly observed at metal/ electrolyte interface, and the following conclusions were derived from the results and discussion.

In Chapter 1, the scope of this study and the composition of this thesis were given.

In Chapter 2, I investigated the decay of homogenous multi-layered islands atop of the terrace on Au (100) and Au(111) single crystals in 0.05 M H_2SO_4 aqueous solution under the control of potential at room temperature by *in-situ* EC-AFM.

The following conclusions were derived from the results and discussion:

1. The area of the first layer of islands decreases linearly with time at any applied potential. From this relationship, it is concluded that the detachment of atoms from the step edge is the limiting process in this decay of islands.
2. When the potential of Au(100) increases in the potential range between 0.15 V and 1.2 V, the decay of islands becomes faster. The decay for Au(111) at 1.05 V is more than 30 times faster than that in air reported. From these results, it is proposed that the metal atoms at metal/electrolyte interface are relaxed toward electrolyte by the electric field at the interface, which becomes higher at higher applied potential.
3. The islands are surrounded by the ledges with high atomic density.
4. The decay for Au(100) at 1.05 V is about 5 times faster than that for Au(111) at the same potential. This difference of the decay rate can be explained by the number of the lateral neighbors of the atom at the kink site and/ or by the effect of the electric field in the electric double layer.
5. The decay of the lower layer before the complete collapse of the upper layer is faster than that after the complete collapse of the upper layer. From this result, it is concluded that this

decay process is mainly caused by the surface diffusion of atoms on the surface from the upper layer to the lower layer, not by the dissolution of atoms at the kink site into solution.

In Chapter 3, the decay of holes made by an AFM cantilever on Ag(100) surface was investigated by in-situ EC-AFM in 0.05 M H_2SO_4 aqueous solution under the control of potential at room temperature. The D_S values were estimated from the EC-AFM observation of the decay and they were compared with those on Au(100) in the same solution. It is found that the D_S values of both Ag(100) and Au(100) increase exponentially with the applied potential. It is also found that the D_S values on Ag(100) were about a hundred times larger than those on Au(100) within the potential range from 0.15 to 0.35 V. From these D_S - E relationships, it is concluded that the activation energy of surface diffusion in aqueous solution decreases when the surface excess charge at metal/electrolyte interface increases.

In Chapter 4, I investigated Cu(110), Cu(100) and Cu(111) surface in 0.1 M $HClO_4$ aqueous solution with or without 10^{-3} M BTAH by *in-situ* EC-AFM and electrochemical methods. From the CVs, I observed that both reactions, Cu dissolution at 0.25 V and H_2 evolution at –0.5 V, were suppressed by the addition of BTAH, except the H_2 evolution on Cu(111). By in-situ EC-AFM, I have observed various ordered structures as shown in Table 4-1. From the anodic polarization measurements, it is found that the breakdown potentials of the BTAH films adsorbed on Cu single crystals in perchloric acid solution are more positive than those in sulfuric acid solution.

In Chapter 5, Fe(110) single crystal electrodes in 0.05 M Na_2SO_4 aqueous solution under the control of potential were investigated by *in-situ* EC-AFM. Keeping the potential at –1.85 V and repeated scanning the surface with the AFM cantilever for 10 minutes yielded to remove the oxide layer off the iron surface and I observed an unreconstructed Fe(110)-(1×1) structure at –1.25 V in 0.05 M Na_2SO_4 aqueous solution. This is the first atomic image of bare Fe(110)-(1×1) obtained in solution. $Fe(OH)_2$(0001)-(1×1) structure of the anodic oxide layer on Fe(110) single crystal was observed at –0.55 V in 0.05 M Na_2SO_4 aqueous solution by *in-situ* EC-AFM. It was found that the anodic oxide layer and Fe(110) substrate had an epitaxial relationship of $Fe(OH)_2$ (0001) $[2\bar{1}\bar{1}0]$ // Fe(110) $[1\bar{1}0]$ and that the misfit between the anodic oxide layer and Fe(110) substrate was less than 1.3%.

In Chapter 6, the electrodeposition in sulfuric acid solution containing both IIb and VIb

elements was investigated by electrochemical methods and X-ray photoelectron Spectroscopy (XPS). The CV in the solution containing both IIb and VIb elements has one cathodic and one anodic peaks which can not observe in the solution containing either IIb or VIb elements, and it is found that these peaks are due to the formation and dissolution of II-VI compound semiconductor. From XPS analysis for the film electrodeposited in the solution containing both Cd and Te at the potential of –1.0 V, where the OPD of Cd does not occur, it is found that this electrodeposited film is mainly composed of CdTe and it's not easily oxidized.

List of Publication

1.**Nobumitsu Hirai,** Hiroaki Tanaka, Shigeta Hara,
Enhanced diffusion of surface atoms at metal/ electrolyte interface under potential control,
Appl. Surf. Sci., Vol.130-132, (1998) pp.506-511.

2. **Nobumitsu Hirai,** Ruxandra Vidu, Toshifumi Tagawa, Shigeta Hara,
Electrodeposition of CdTe Thin Films on Au(111)/Polyethylene (in Japanese),
Journal of the Surface Science Society of Japan, Vol.20, No.4, (1999) pp.228-234.

3. **Nobumitsu Hirai,** Hideki Sano, Shigeta Hara,
In Situ AFM Investigation of Benzotriazole Adsorbed on Cu(110) in Perchloric Acid Solution,
Electrochemistry, Vol.67, No.12, (1999) pp.1120-1122.

4. **Nobumitsu Hirai,** Ken-ichi Watanabe, Akiko Shiraki, Shigeta Hara,
In-situ AFM observation on the decay of small islands on Au single crystal in acid Solution,
J. Vac. Sci. Technol. B, Vol.18, No.1, (2000) pp.7-9.

5. **Nobumitsu Hirai,** Shigeta Hara,
Surface Diffusion of Metal in Contact with Aqueous Solution under Controlled Potential (in Japanese),
Molten Salts (ISSN No. 0916-1589), Vol. 43, No. 1, (2000) pp.7-16.

6. **Nobumitsu Hirai**, Hiromi Okada, Shigeta Hara,
In Situ Electrochemical Atomic Force Microscopy with Atomic Resolution of Fe(110) in Sodium Sulfate Aqueous Solution,
ISIJ International (accepted on March 8, 2000), Vol. 40, No. 7, (2000), in press.

Acknowledgements

I wish to express my deepest thanks to Professor Shigeta Hara of Osaka University for his warm guidance, constructive discussion and encouragement.

I express my sincere thanks to Professor Toshio Shibata of Osaka University and Professor Masahiko Yamamoto of Osaka University for critically reviewing this thesis.

I wish to thank to Professor Toshihiro Tanaka, Professor Shinji Fujimoto and Dr. Jürgen Walter for their kind and helpful discussion during the period of my work.

I acknowledge Dr. Yasuhide Nakayama, Dr. Yoshiaki Yamaguchi and Dr. Masashi Shiota of Yuasa Corporation for supporting my work.

I thank the students of Professor S. Hara's group for their experimental assistance.

I am very grateful to Professor Isao Yamada of Kyoto University and Professor Hiroyuki Matsunami of Kyoto University for their kind guidance and encouragement during my days of my graduate and undergraduate schools of Kyoto University.

I am deeply indebted to Professor Atsushi Nishiwaki of Osaka University for his warm and continuous encouragement.

I appreciate sincerely to my wife Tomoo, my son Yoshitake, my father Hiroshi, my mother Kyoko, my grandparents and my best friends for their continuous encouragement and moral support.